Materials Today Communications 48 (2025) 113442

Contents lists available at ScienceDirect

Materials Today Communications

journal homepage: www.elsevier.com/locate/mtcomm

Zr-enhanced ambient-air thermal oxidation of Ti–30Zr–5Mo alloy using low T_β for implants

Yiming Jin [a], Jiani Li [a], Takayoshi Nakano [d], Hideki Hosoda [e], Mitsuo Niinomi [d,g], Xiaowei Zhang [f], Deliang Zhang [a], Xiaoli Zhao [a,b,c,*]

[a] School of Materials Science and Engineering, Northeastern University, Shenyang 110819, PR China
[b] National Frontiers Science Center for Industrial Intelligence and Systems Optimization, Northeastern University, Shenyang 110819, PR China
[c] Key Laboratory of Data Analytics and Optimization for Smart Industry (Ministry of Education), Northeastern University, Shenyang 110819, PR China
[d] Division of Materials and Manufacturing Science, Graduate School of Engineering, Osaka University, 2-1, Yamadaoka, Suita, Osaka 565-0871, Japan
[e] Laboratory for Future Interdisciplinary Research of Science and Technology & Materials and Structures Laboratory, Institute of Integrated Research (IIR), Institute of Science Tokyo, Yokohama 226-8501, Japan
[f] Western Titanium Technologies Co., Ltd, Xi'an 710201, PR China
[g] Institute for Materials Research, Tohoku University, Sendai 980-8577, Japan

ARTICLE INFO

Keywords:
Ti–30Zr–5Mo alloy
Thermal oxidation
Oxidation mechanism
Internal oxidation
Surface modification

ABSTRACT

Metastable β-Ti alloy Ti–30Zr–5Mo ($T_\beta \approx 700$ °C) offers low modulus, biocompatibility, and strength for spinal rod implants but has limited hardness (280 Hv) and wear resistance. Conventional surface treatments like vacuum-based physical vapor deposition (PVD), are costly and complex. This study exploits the low T_β and high Zr content (30 wt%) of Ti–30Zr–5Mo alloy for single-step, ambient-air thermal oxidation at 600–700 °C, combining heat treatment with surface modification. The low T_β ensures controlled oxidation, preventing over-oxidation, while Zr's selective oxidation forms a dense ZrO_2-rich layer, which is harder than TiO_2, enhancing surface hardness. Spontaneous tetragonal to monoclinic phase transitions in ZrO_2 further improve toughness. The resulting 5 μm-thick oxide layers exhibit a threefold hardness increase (904 Hv vs. 280 Hv), a surface roughness of 0.30 μm (suitable for osseointegration), strong interfacial adhesion (critical load: 43 N), and an 18-fold reduction in corrosion current density (from 1.62×10^{-7} to 8.96×10^{-9} A·cm^{-2}). Despite minor microcracks, the layers maintain structural integrity, offering exceptional durability. This atmosphere-free approach provides a scalable solution for orthopedic and dental implants, combining mechanical durability with biological integration. The insights into Zr-driven oxidation dynamics at low T_β could inform vacuum-based processes, when controlled oxygen partial pressure might further optimize oxide layer properties, aligning with advancement in surface technology.

1. Introduction

Titanium alloys, particularly β-type alloys, are widely recognized as promising materials for biomedical applications, such as surgical implants, due to their high specific strength, excellent corrosion resistance, biocompatibility, and low elastic modulus [1,2]. Recent research on β-type titanium alloys, such as Ti–Mo, Ti–Zr, and Ti–Nb–Ta, focuses on enhancing phase stability, incorporating biocompatible alloying elements (e.g., Mo, Zr, Ta), and tailoring microstructures to balance low modulus with mechanical strength for long-term implant reliability [3,4]. Among these, Ti–Zr alloys have gained attention for their enhanced mechanical properties and reduced Young's modulus, making them suitable for load-bearing implants [5,6]. However, alloys with low Zr content are particularly susceptible to pitting corrosion in chloride-rich environments, such as the human body, can lead to the release of metallic ions and inflammatory responses, limiting their long-term performance [7]. To address this challenge, recent research has focused on incorporating non-toxic β-stabilizing elements like molybdenum (Mo) to improve the mechanical and corrosion properties of Ti–Zr alloys [8]. Recent studies [9–13] show Ti–30Zr–5Mo's low elastic modulus, biocompatibility, and stress-induced α′ martensitic transformation, driven by its low β-transus temperature and high Zr content, ideal for spinal rods. For instance, the alloy's yield-to-tensile strength ratio (0.3–0.9) and tensile strengths up to 1110 MPa can be tailored by

* Corresponding author at: School of Materials Science and Engineering, Northeastern University, Shenyang 110819, PR China
E-mail address: zhaoxl@mail.neu.edu.cn (X. Zhao).

https://doi.org/10.1016/j.mtcomm.2025.113442
Received 16 May 2025; Received in revised form 15 July 2025; Accepted 27 July 2025
Available online 28 July 2025

adjusting the α phase content through thermal or mechanical processing, enabled by its low β-transus temperature and high Zr content [10]. Heat treatment at carefully selected temperatures not only optimizes the α/β phase balance for superior mechanical properties but also promotes surface oxidation, achieving structure–function integration. While prior studies on Ti–30Zr–5Mo alloy emphasized mechanical performance and corrosion, surface modifications for enhanced reliability remain underexplored. Our single-step thermal oxidation integrates microstructure control with a TiO_2–$ZrTiO_4$–ZrO_2 layer, leveraging ZrO_2's superior surface durability for implant longevity.

Surface modification is critical for enhancing the performance of titanium alloys in biomedical applications, as the native oxide layer on these alloys is typically thin and insufficient for optimal osseointegration [14]. Various techniques have been developed to improve surface properties, including vacuum-based methods like plasma electrolytic oxidation and physical vapor deposition (PVD), which offer precise control over film growth and composition [15,16], as well as atmospheric methods like micro-arc oxidation and thermal oxidation [17,18]. In line with these developments, recent surface modification trends focus on methods such as thermal oxidation, plasma nitriding, and hydroxyapatite coatings, which are designed to enhance corrosion resistance, wear behavior, and biological integration [19–21]. However, vacuum-based techniques are costly, and the low β-transus temperature ($T_\beta \approx 700$ °C) of metastable β-Ti alloys pose thermal instability risks during high-temperature processing. This study exploits the low T_β of Ti–30Zr–5Mo alloy, a common trait of β-Ti alloys, in combination with its high Zr content (30 wt%) to enable a single-step ambient-air thermal oxidation process at 600–700 °C that integrates heat treatment and surface modification. The low T_β ensures controlled oxidation, preventing over-oxidation, While Zr's selective oxidation forms a dense ZrO_2-rich internal oxide layer-harder than TiO_2-enhancing surface hardness. Stress-induced tetragonal-to-monoclinic phase transformation in ZrO_2 further improve toughness, making this approach a cost-effective and scalable solution.

This study investigates the thermal oxidation mechanism and behavior of the Ti–30Zr–5Mo alloy, focusing on the effects of oxidation time and temperature on the phase constituents, morphology, and surface properties of the oxide layers. By examining the internal oxidation kinetics and growth mechanisms, this research aims to develop dense oxide layers with high hardness and strong substrate adhesion, providing valuable insights for advancing biomedical Ti–Zr–Mo alloys. Furthermore, the findings offer potential implications for vacuum-based processes, where controlled oxygen partial pressure could further optimize oxide layer properties, aligning with the scope of vacuum science and surface technology.

2. Experiment

2.1. Materials preparation

The Ti–30Zr–5Mo alloy, a metastable β titanium alloy, was prepared by proportioning titanium sponge, zirconium sponge, and high-purity molybdenum blocks to the target composition. The mixture was melted three times into 80 mm diameter ingots using vacuum levitation melting, homogenized at 1100 °C for 12 h, forged at the same temperature, and air cooled. The chemical composition of the forged alloy is listed in Table 1. Specimens with dimensions of 10 mm× 10 mm× 2 mm were sectioned using wire electrical discharge machining (WEDM). The largest face of each sample was polished with SiC abrasive papers (grit #80 to #5000) and non-oxidized surfaces were coated with a high-temperature-resistant silica-based paste to prevent unwanted oxidation; this coating was removed by ultrasonic cleaning in ethanol after oxidation. Samples were cleaned in ultrasonic baths of acetone and alcohol, then dried. Each sample was weighed using an electronic analytical balance (accuracy: 0.10 mg), with eight measurements averaged per sample. The dimensions of the oxidized surfaces were measured using a vernier caliper, averaging five measurements per sample Fig. 1.

Table 1
The chemical composition of Ti–30Zr–5Mo alloy (in wt%).

Element	Zr	Mo	O	N	Ti
Content	28.9	4.93	0.016	0.007	Bal.

2.2. Thermal oxidation

Thermal oxidation experiments were conducted in a low-temperature muffle furnace (SX-GO7103) in an air atmosphere. For isochronous oxidation, samples were heated to 600 °C, 650 °C, 680 °C, 700 °C, and 850 °C for 1 h, followed by ice-water quenching. The selected temperature range (600–850 °C) spans both below and above the β-transus ($T_\beta \approx 700$ °C). Below T_β, moderate α phase precipitation occurs, strengthening the β matrix and influencing oxidation behavior. Above T_β, higher oxygen diffusivity promotes the formation of thicker oxide layers, despite some surface exfoliation. This range thus enables simultaneous regulation of the alloy's microstructure and the formation of functional oxide layers. For isothermal oxidation, 600 °C was chosen to ensure controlled oxidation and minimal microstructural impact, with samples oxidized for 1, 2, 3, 4, 5, and 7 h, followed by ice-water quenching.

2.3. Characterization of oxide layers

The cross-sectional morphology of the oxide layers and substrate was analyzed using a field emission scanning electron microscope (FESEM, JEOL JSM-7001F). The oxide layer thickness was determined as the average of 50 cross-sectional measurements per sample. Interface undulations are defined by amplitude (height variation between peaks and troughs) and wavelength (distance between peaks), quantified using Image J software to analyze local oxide thickness deviations (±10 % of the mean thickness) across 12 SEM cross-sectional images per sample at 4 μm intervals [22]. This characterization assesses oxide-substrate interface morphology, influencing adhesion and corrosion resistance. The elemental composition of the internal oxide layer was determined using an energy-dispersive spectrometer (EDS; Bruker QUANTA XFlash730). The phase constituents of surface oxide layers were characterized by X-ray diffraction (XRD, Smart Lab, Rigaku) using Cu K_α radiation (λ=1.5406 Å) at 40 kV and 200 mA, with θ-2θ scans from 20° to 90° (2θ) at 6° min^{-1} (step size: 0.02°, counting time: 0.5 s/step). The chemical states of surface elements in the external oxide layer were analyzed by X-ray photoelectron spectroscopy (XPS, PH II Quantera II). The Vickers hardness was measured using a digital micro-Vickers hardness tester (401MVD) with a 25-gf load and 10-second holding time. The average hardness was calculated from 12 measurements per sample, with a minimum spacing of 200 μm. Surface roughness (R_a) was determined using a laser confocal microscope (OLS3100), averaging 10 measurements per sample. The adhesive strength between the oxide layer and substrate was evaluated using a multi-functional material surface property tester (MFT-4000) with a round diamond indenter (cone angle: 120°, radius: 200 μm). A dynamic load increasing from 0.2 N to 100 N at 100 N/min was applied, with four scratch tests per sample. Scratch morphology was analyzed using a scanning electron microscope (JSM-6510), and the critical load was determined from abrupt changes in the loading-friction acoustic emission curves. Electrochemical corrosion tests were performed using a PARSTAT 3000 A electrochemical workstation with a standard three-electrode system, consisting of a saturated calomel electrode (SCE) as the reference, a platinum counter electrode, and the specimen as the working electrode (exposed area: 100 mm^2) in naturally aerated 0.9 wt% NaCl solution at 23 ± 2 °C. Oxidized (650 °C, 1 h) and oxide-free Ti–30Zr–5Mo samples were mechanically polished (lightly for oxide-covered surfaces),

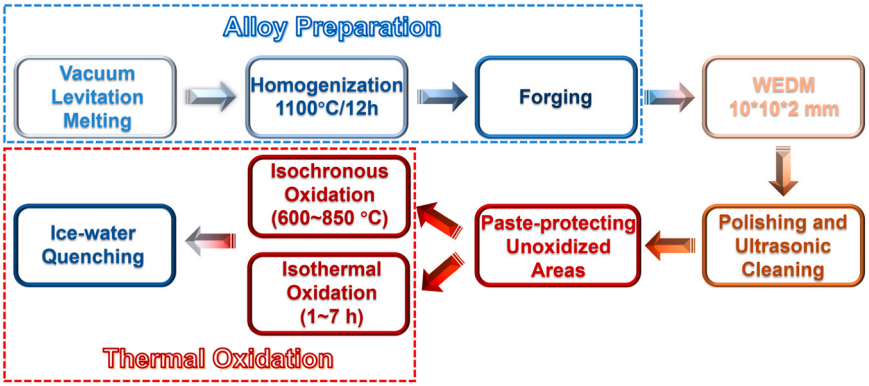

Fig. 1. Schematic of Ti–30Zr–5Mo alloy preparation (melting, casting), heat treatment, WEDM shaping, and thermal oxidation (600–850 °C) for biomedical implants.

ultrasonically cleaned in ethanol, and sealed to define test area. Open circuit potential (OCP) was monitored for 3600 s until stabilization. Electrochemical impedance spectroscopy (EIS) used 10 mV RMS over a frequency range of 10^5–10^{-2} Hz. Potentiodynamic polarization (PDP) scans were conducted from −1.30 V to + 1.50 V versus SCE at a scan rate of 0.333 mV/s, following ASTM G5 protocol for anodize polarization analysis. All measurements were performed in quadruplicate to ensure reproducibility. Surface morphology after corrosion testing was examined using a field emission scanning electron microscope (FESEM, JEOL JSM-7001F).

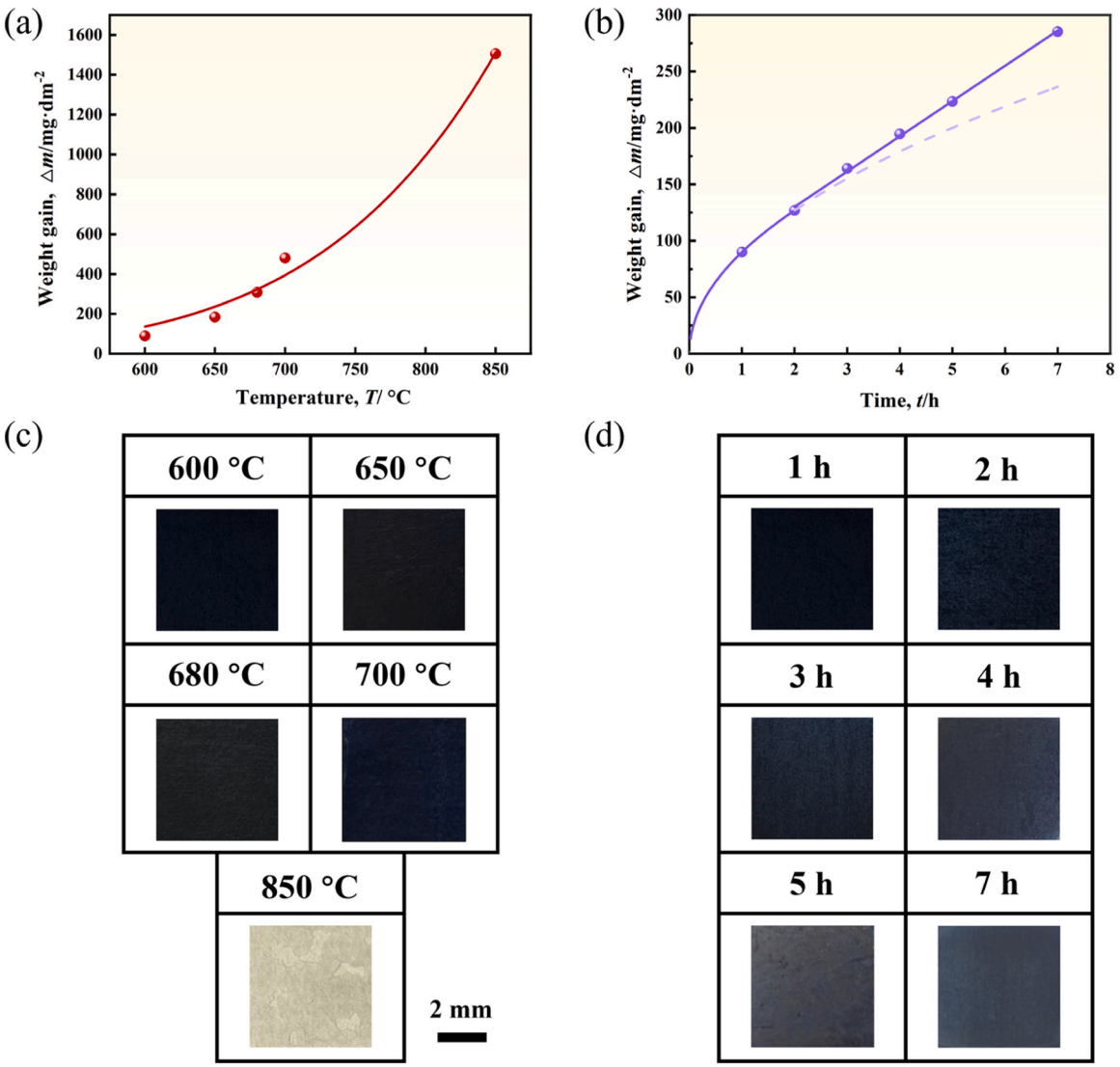

Fig. 2. Weight gain of Ti–30Zr–5Mo materials and the surface color and morphology after oxidation: (a, c) Isochronous oxidation at 600–850 °C for 1 h; (b, d) Isothermal oxidation at 600 °C for durations ranging from 1 to 7 h.

3. Results

3.1. Surface colors of the oxide layers and oxidation behavior

The surface color and macroscopic morphology of oxide layers provide a rapid assessment of their quality, which influences both functional properties and aesthetic appeal. This study investigated the variation in surface color of the oxide layers on Ti–30Zr–5Mo alloy under different thermal oxidation parameters, combining surface color analysis with weight gain trends to evaluate oxidation behavior.

Fig. 2(a) and (c) show the weight gain and surface morphologies of Ti–30Zr–5Mo materials after isochronous oxidation at 600–850 °C for 1 h. After oxidation at 600–700 °C for 1 h, the material surfaces remain smooth and flat, with oxide layers firmly adhering to the substrate. As the oxidation temperature increases, the surface color transitions from deep black to black. However, at 850 °C, the oxide layer exhibits significant cracking and spalling, compromising its structural integrity and potentially affecting weight measurements. The surface color shifts to light yellow, indicating pronounced changes in the oxide layer. The oxidation weight gain follows a parabolic trend with temperature, with a sharp increase above 680 °C and a pronounced surge between 700 °C and 850 °C, highlighting an intensified oxidation reaction at higher temperatures and correlating with the observed color changes.

Fig. 2(b) and (d) present the weight gain and corresponding surface morphologies after isothermal oxidation at 600 °C for durations ranging from 1 to 7 h. During the 7-hour isothermal oxidation, the surface remains smooth, uniform, and intact, with the oxide layer adhering firmly to the alloy substrate. As oxidation time increases, the surface color progressively lightens, transitioning from deep black to black, then dark gray, and finally gray. Weight gain exhibits a parabolic trend in the first two hours, indicating a decelerating oxidation rate, followed by a linear trend, suggesting an accelerated rate. These findings indicate the significant influence of both temperature and duration on the oxidation behavior of the alloy, necessitating a detailed evaluation of the oxide layer's microscopic morphology and properties to optimize oxidation conditions.

3.2. Microscopic morphology of the oxide layers

Fig. 3 illustrates the microstructural evolution of the Ti–30Zr–5Mo alloy under 1-hour oxidation. The as-forged alloy consists of fine acicular α phases (60 % volume fraction, 0.03 μm width) within a β matrix. At 600–680 °C, the α phases coarsen (width increasing to 0.05–0.26 μm) and partially dissolve, reducing their volume fraction to 50–20 %. Above the β transus (~700 °C), the α phases fully dissolve, yielding a β-phase microstructure with coarsened grains (300 μm at 850 °C). The α/β phase ratio significantly influences surface oxidation: the Ti-rich α phase accelerates TiO_2 formation due to higher reactivity, while the Mo-stabilized β phase slows oxidation kinetics, enhancing oxide layer adhesion. At higher temperatures, the β-dominated microstructure helps reduce oxide growth rates, improving oxidation resistance.

Fig. 4 depicts the cross-sectional morphologies of Ti–30Zr–5Mo

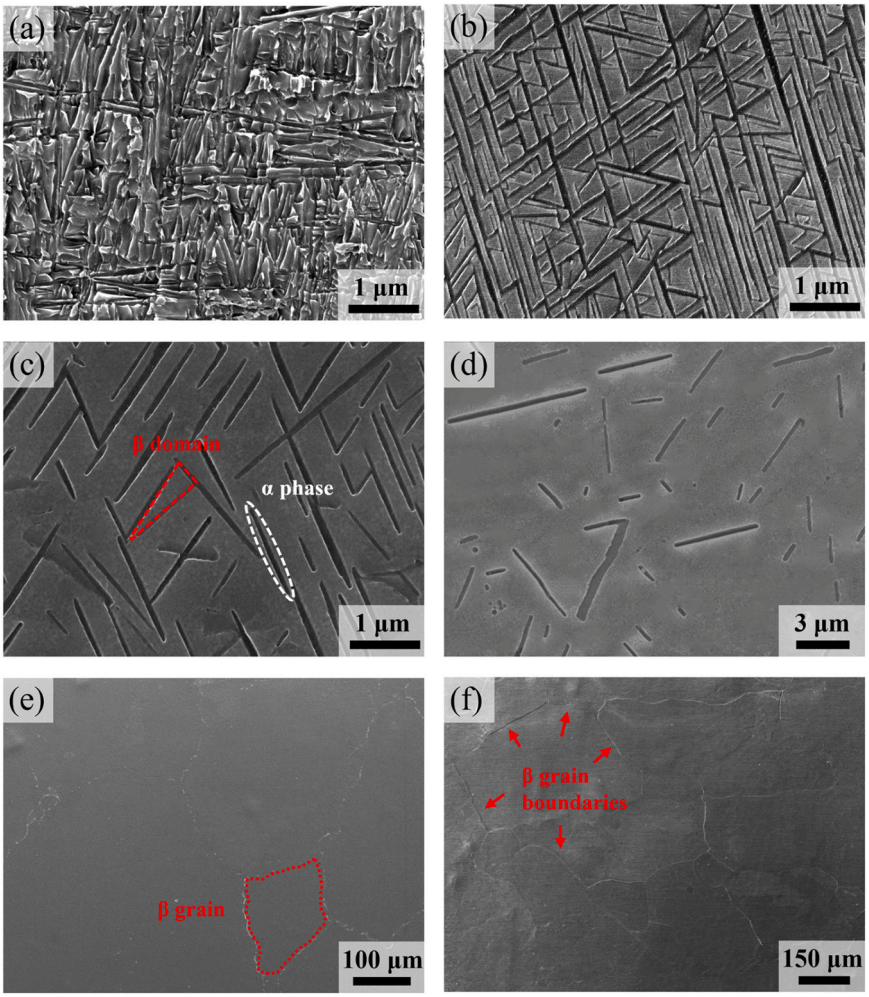

Fig. 3. SEM micrographs showing microstructural evolution of the Ti–30Zr–5Mo alloy before and after 1-hour oxidation at increasing temperatures: (a) As-forged (unoxidized), (b) 600 °C, (c) 650 °C, (d) 680 °C, (e) 700 °C and (f) 850 °C.

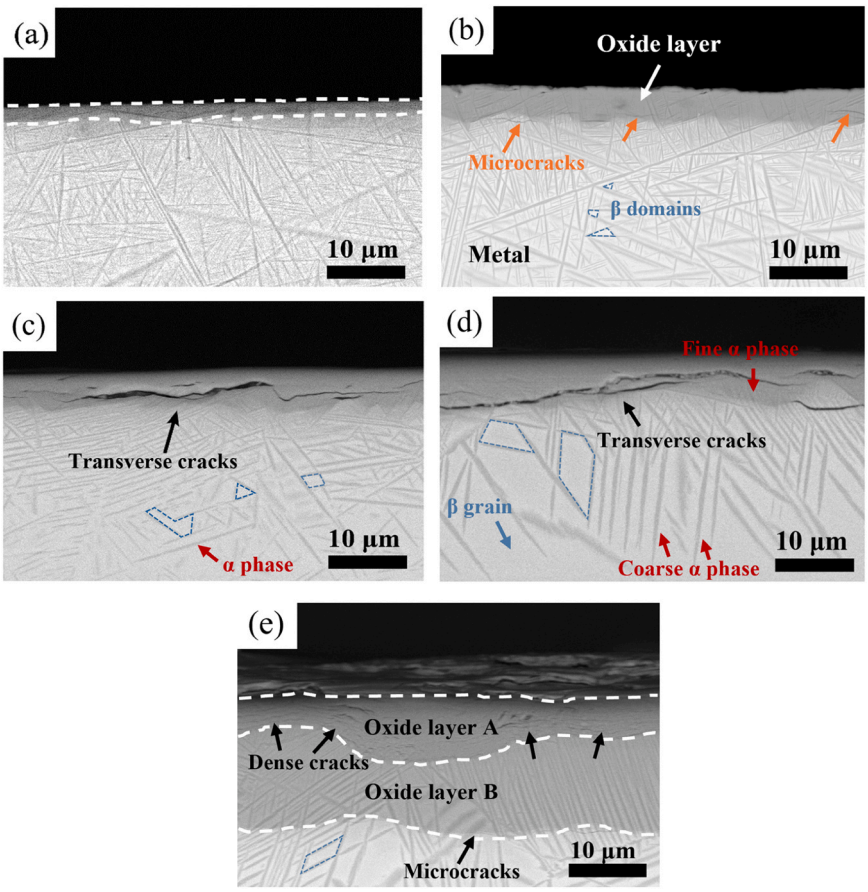

Fig. 4. Cross-sectional morphologies of Ti–30Zr–5Mo materials after 1-hour isochronous oxidation at various temperatures: (a) 600 °C, (b) 650 °C, (c) 680 °C, (d) 700 °C and (e) 850 °C.

materials after isochronous oxidation for 1 h. The α phases within the internal oxide layer are notably refined due to an oxygen gradient from the oxide layer to the substrate interior, driven by oxygen diffusion during oxidation. Oxygen forms an interstitial solid solution with titanium, and the segregation of interstitial atoms at grain boundaries impedes grain growth, with the effect intensifying at higher oxygen concentrations. Additionally, oxygen raises the β transus temperature, increasing the disparity between the oxidation temperature and the phase transformation temperature, as reflected by the variation in phase composition between the substrate and near-surface regions.

At 600–650 °C, Fig. 4(a) and (b) show a low-contrast subsurface zone indicating internal oxidation, supported by XRD (*m*-ZrO_2, $ZrTiO_4$) and EDS (~38 at% oxygen difference). For load-bearing implants, particulate debris from microcracks in oxide or hydroxyapatite coatings can trigger inflammation, osteolysis, and aseptic loosening, reducing implant longevity [23]. Thermal oxidation at 600–650 °C produces a dense, adherent ZrO_2 layer (2–5 μm thick) with minimal subsurface microcracks that do not compromise performance. This oxide layer maintains strong interfacial integrity, reducing the risk of particle-induced inflammation, and is well-suited for biomedical applications requiring stable, biocompatible surfaces. The internal oxide layer retains the crystal structure of the metallic substrate [24], adheres firmly to the substrate, and exhibits a smooth surface after isochronous oxidation, though irregular fluctuations are observed at the interfaces. As the temperature increases, the oxide layer thickness increases, but its internal structure becomes looser, with cracks forming that reduce its protective effectiveness. At higher temperatures, internal stresses escalate due to volume mismatch between the oxides and the consumed metal, phase transformations, and differences in the thermal expansion coefficients between the oxide and metal. These stresses, which intensify with increasing oxide layer thickness, eventually exceed the material's stress tolerance, triggering crack initiation [25]. Consequently, transverse cracks develop within the oxide layers and at the interfaces, increasing in number and size with temperature, particularly at interface undulations where stress concentrations are higher.

At 850 °C, the oxide layer morphology changes significantly, forming two distinct oxide layers with an uneven surface. The outer oxide layer (oxide layer A) exhibits a loose, lamellar structure with numerous fine transverse cracks, while the inner oxide layer (oxide layer B) is dense, with minimal cracking but noticeable undulations at the interface between the two layers. The oxide layer/substrate interface shows reduced undulations with a few microcracks. The phase constitution of these oxide layers is analyzed in Section 3.3 using XRD patterns.

Fig. 5(a) quantifies the wavelength and amplitude of surface undulations induced by isochronous oxidation. The amplitude, remaining below 25 % of the oxide layer thickness, increases initially, decreasing slightly at higher temperatures, then rises again, while the wavelength increases continuously with temperature, indicating a more homogeneous oxide distribution that suppresses further oxidation in advanced stages. Fig. 5(b) demonstrates that the oxide layer thickness increases progressively with temperature, growing from ~2.1 μm at 600 °C to ~5.4 μm at 650 °C, ~9.3 μm at 700 °C, and sharply to ~27.3 μm at 850 °C. Specifically, between 680 °C and 700 °C, the growth rate moderates as the internal oxide layer become sufficiently thick to impede oxygen diffusion, enhancing its protective effect.

Fig. 6 shows stable α phase width and distribution after oxidation at 600 °C for varying durations, indicating minimal microstructural changes. This stability enables analysis of oxide layer growth kinetics, independent of microstructural evolution.

The cross-sectional morphologies of Ti–30Zr–5Mo materials after

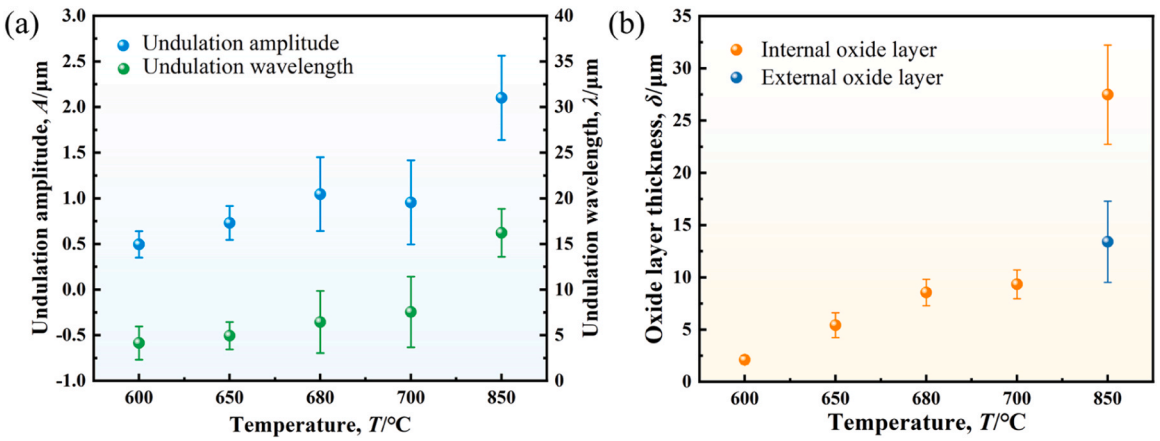

Fig. 5. (a) Variations in amplitude and wavelength of undulations at the internal oxide layer/metal interface after isochronous oxidation. (b) Oxide layer thickness after isochronous oxidation.

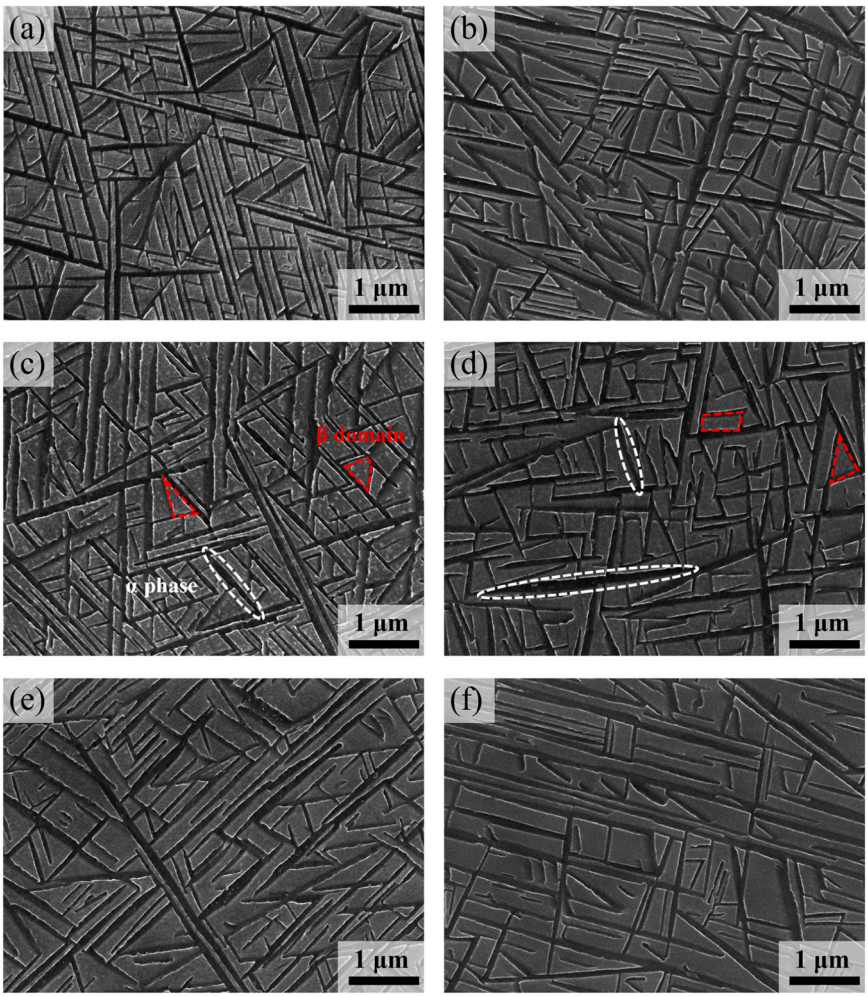

Fig. 6. SEM micrographs of the Ti–30Zr–5Mo alloy microstructure after isothermal oxidation at 600 °C for varying durations: (a) 1 h, (b) 2 h, (c) 3 h, (d) 4 h, (e) 5 h and (f) 7 h.

isothermal oxidation at 600 °C for varying durations are shown in Fig. 7. At low temperature, oxygen diffusion into the substrate is slow, resulting in minimal increases in oxide layer thickness. Microcracks form at the oxide layer /substrate interface after 2 h, increasing in number and length with extended oxidation time. After 7 h, numerous small cracks appear within the oxide layer, though compressive stress partially suppresses crack propagation. As illustrated in Fig. 8, the oxide layer thickness remains stable for the first 2 h, then increases significantly, with an accelerating growth rate over longer durations, reaching approximately 3.7 μm after 7 h. These values, averaged from 50 cross-sectional measurements, show high variability due to non-uniform oxygen diffusion driven by the heterogeneous α and β phase

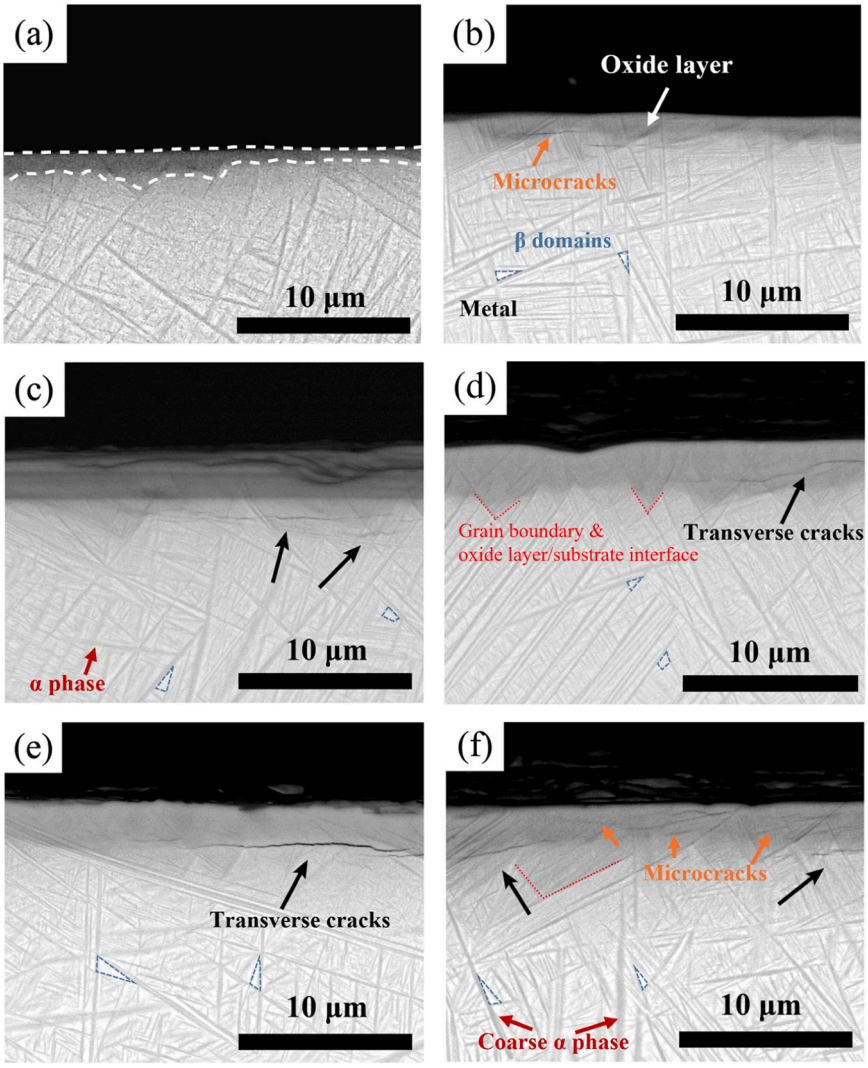

Fig. 7. Cross-sectional morphologies of Ti–30Zr–5Mo materials after isothermal oxidation at 600 °C for various durations: (a) 1 h, (b) 2 h, (c) 3 h, (d) 4 h, (e) 5 h, and (f) 7 h.

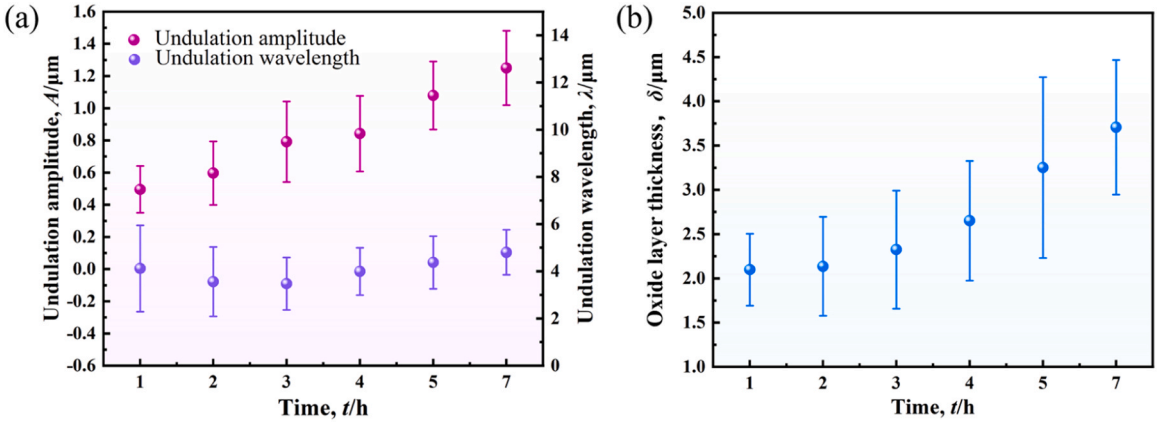

Fig. 8. (a) Variations in amplitude and wavelength of undulations at the oxide layer/metal interface after isothermal oxidation. (b) Oxide layer thickness after isothermal oxidation.

microstructure, resulting in variable interface waviness and oxide thickness. The undulation amplitude at the interface increases rapidly after 2 h, while the wavelength decreases until 3 h. Higher standard deviations in undulation parameters suggest variability in the magnitude and distribution [22], likely due to differing oxygen diffusion rates influenced by oxidation layer densification and the uneven oxide distribution.

3.3. Phase constituents of the oxide layers

Fig. 9(a) presents the XRD patterns of Ti–30Zr–5Mo materials oxidized at 600 °C to 850 °C for 1 h. At temperatures below 700 °C, the presence of prominent diffraction peaks corresponding to the substrate phases can be attributed to two factors: partial retention of metallic phases within the internal oxide layer, and the limited thickness of the oxide layers, which allows X-rays to penetrate through to the underlying substrate [26]. The substrate consists of α and β phases, with diffraction peaks shifts leftward relative to the PDF standard cards, likely due to lattice distortions from oxygen and zirconium incorporation. The β transus temperature of the Ti–30Zr–5Mo alloy is approximately 700 °C [12]. The presence of α phases above 700 °C results from oxygen diffusion, which creates concentration gradient from the surface to the substrate interior, increasing the β transus temperature near the oxide layer and facilitating α phase precipitation when oxygen exceeds a critical threshold [27]. As oxygen diffusion continues, the boundary between the α+ β phase and β phase regions migrates inward [28]. The oxide constitution varies with temperature: below 650 °C, the oxides primarily consist of monoclinic zirconia (m-ZrO_2) and $ZrTiO_4$; at 680–700 °C, weak diffraction peaks of rutile titanium dioxide (r-TiO_2) appear; at 850 °C, external oxidation intensifies, with prominent peaks of r-TiO_2, tetragonal zirconia (t-ZrO_2), and $ZrTiO_4$.

The Ellingham-Richardson diagram indicates that the equilibrium partial pressure of oxygen at the Zr/ZrO_2 interface is lower than at the Ti/TiO_2 interface, suggesting Zr's higher reactivity in an oxygen-rich environment. However, as Zr concentration in the alloy is below the critical threshold for transitioning from internal to external oxidation, ZrO_2 precipitates within the alloy substrate [29]. During the thermal oxidation, Zr preferentially reacts with oxygen to form t-ZrO_2, followed by r-TiO_2 formation within the t-ZrO_2 lattice. Since both t-ZrO_2 and r-TiO_2 possess tetragonal crystal structure, they form a solid solution as oxidation progresses [30]. Internal stress from volume mismatch between the oxide and metal stabilizes the t-ZrO_2 structure, despite its instability at lower temperature. As shown in Fig. 9(c), below 700 °C, Ti plays a significant role in the oxidation, with the $ZrTiO_4$ phase content

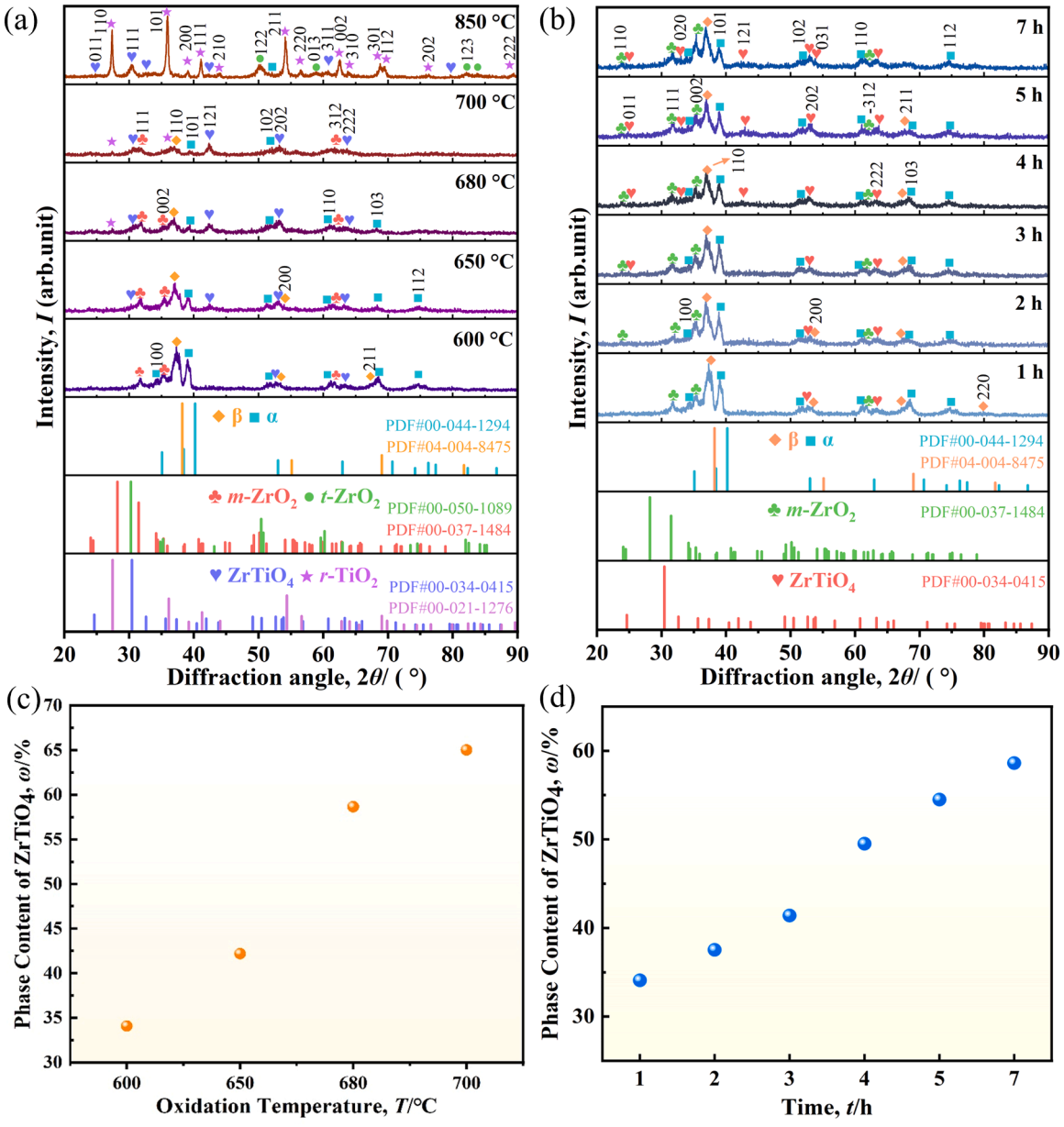

Fig. 9. (a) XRD pattern of materials oxidized at 600–850 °C for 1 h. (b) XRD pattern of materials oxidized at 600 °C for 1–7 h. (c) $ZrTiO_4$ phase content after isochronous oxidation. (d) $ZrTiO_4$ phase content after isothermal oxidation.

increasing with temperature, highlighting the interplay among Ti, Zr, and oxygen during oxidation, with the $ZrTiO_4$ content peaking approximately 65.0 %.

Fig. 9(b) shows XRD patterns of Ti–30Zr–5Mo oxidized at 600°C for 1–7 h, revealing $ZrTiO_4$, and *m*-ZrO_2 phases. For isothermal oxidation at 600 °C, even after 7 h, the XRD patterns show strong substrate phase peaks with minimal change, indicating that temperature has greater effect on oxidation behavior than time within this timeframe. As oxidation time increases, the intensity of *m*-ZrO_2 and $ZrTiO_4$ peaks increase, reflecting a higher $ZrTiO_4$ content in the oxide layer, as depicted in Fig. 9(d), with an increase of approximately 24.5 % from 1 to 7 h. The phase composition evolution, derived from XRD patterns, is discussed in Sections 4.2 and 4.3, within the context of phase transformations and oxidation mechanisms.

EDS mapping and line scans of cross-sections oxidized at 650 °C for 1 h, 850 °C for 1 h, and 600 °C for 7 h (Fig. 10) reveal oxide layer composition. Ti, Zr, Mo, and O distributions clearly distinguish the internal oxide layer from the substrate, with oxygen enriched by ~38 at% in the oxide layer formed at 650 °C for 1 h compared to the substrate 2 μm below. This confirms the presence of both oxides and alloy substrate within the internal oxide layer, with oxygen existing as a solid solution in the substrate, as part of oxides, and as non-stoichiometric defects within the crystal structure [31]. At 850 °C, EDS line scans across the outer oxide layer show pronounced fluctuations in Mo concentration due to redistribution between α and β phases and α grain coarsening. High-resolution XPS further validates the outer oxide's chemical state, as discussed at the end of this section.

At 850 °C, a double-layer oxide structure forms within 1 h, as shown in Fig. 4(e). After removing the outer oxide layer (layer A), the inner oxide layer (layer B) was analyzed by XRD (Fig. 11). Strong diffraction peaks of $ZrTiO_4$ and *t*-ZrO_2, along with weak peaks of *m*-ZrO_2 and *r*-TiO_2, indicate that $ZrTiO_4$ and *t*-ZrO_2 are the dominant phases in layer B, based on PDF standard cards (#00–034–0415 for $ZrTiO_4$, #00–050–1089 for *t*-ZrO_2). As oxidation progresses, *t*-ZrO_2 grains grow to a critical size, triggering a martensitic phase transformation to *m*-ZrO_2, facilitated by reduced internal stresses due to the external oxide

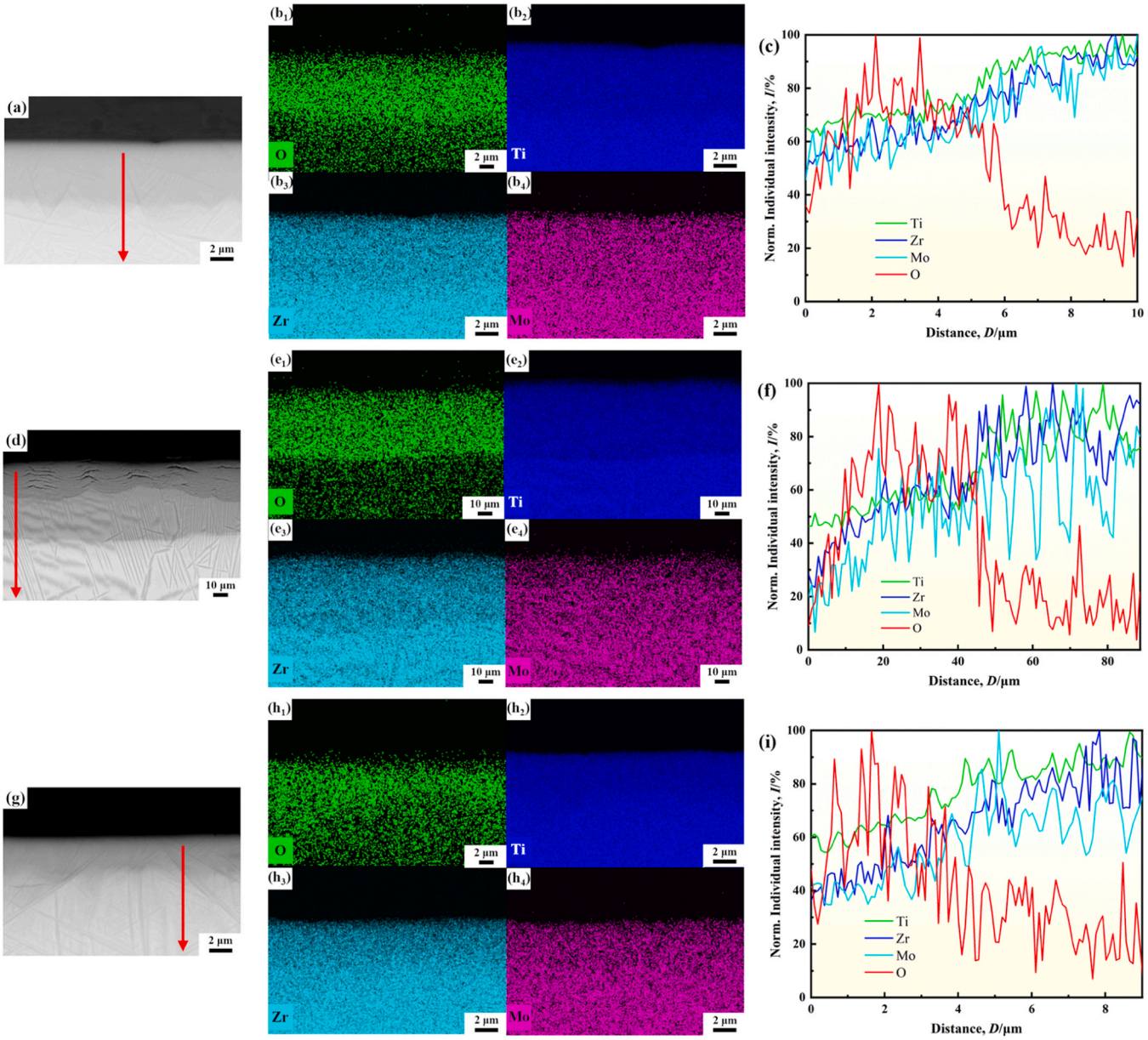

Fig. 10. Cross-sectional EDS mapping and line scan analyses (c, f, and i) of Ti–30Zr–5Mo alloy after thermal oxidation: (a–c) 650 °C for 1 h, (d–f) 850 °C for 1 h and (g–h) 600 °C for 7 h.

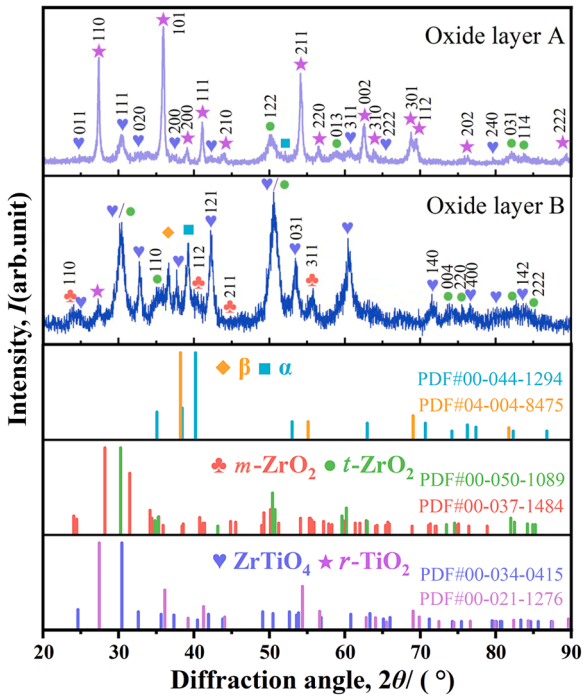

Fig. 11. XRD pattern of the double oxide layer formed at 850 °C for 1 h.

layer formation, leading to *m*-ZrO_2 detection in layer B [32]. The presence of $ZrTiO_4$ and *t*-ZrO_2 in layer B reflects the poor integrity and non-protective nature of the TiO_2 layer in layer A.

To further investigate the chemical states of elements in external oxide layer, high-resolution X-ray photoelectron spectroscopy (XPS) was conducted for Ti, Zr, Mo, and O, with spectra calibrated to the C 1 s peak at 284.8 eV. As shown in Fig. 12(a), the Ti 2p spectrum exhibits a characteristic doublet at 458.4 eV (Ti $2p_{3/2}$) and 464.1 eV (Ti $2p_{1/2}$), with a spin-orbit splitting of 5.7 eV, indicative of the Ti^{4+} state in TiO_2. A weak shoulder at 459.2 eV suggests localized spallation of the outer oxide layer or cracking-induced exposure of the metallic Ti substrate. The Zr 3d spectrum in Fig. 12(b) exhibits peaks at 181.3 eV (Zr $3d_{5/2}$) and 183.7 eV (Zr $3d_{3/2}$), confirming the Zr^{4+} state. The Mo 3d spectrum in Fig. 12(c) reveals a 3.2 eV spin-orbit splitting, with peaks at 232.1 eV (Mo $3d_{5/2}$) and 235.3 eV (Mo $3d_{3/2}$), corresponding to the Mo^{6+} state. Quantitative analysis indicates that MoO_3 constitutes 5.9 % of the oxide layer, indicating trace oxide formation despite Mo's high-temperature oxidation resistance. Fig. 12 shows Ti^{4+}, Zr^{4+}, and Mo^{6+} in the external oxide layer, indicating stable oxide formation via outward cation diffusion during high-temperature oxidation. The predominance of Ti^{4+} and Zr^{4+}, forming chemically stable, high-lattice-energy oxides, ensures excellent resistance to further oxidation and minimal solubility in acidic and alkaline conditions [33], supporting the alloy's suitability for spinal rod applications. The O 1 s spectrum in Fig. 12(d) resolves two components: a dominant peak at 529.7 eV, assigned to lattice oxygen (O^{2-}) and a secondary peak at 531.6 eV, attributed to surface hydroxyl groups (–OH). These hydroxyl groups, linked to non-equilibrium oxygen vacancy defects from rapid quenching, enhance surface reactivity, promoting water molecule adsorption and hydroxylation [34]. This defect-engineered surface improves hydrophilicity and biological

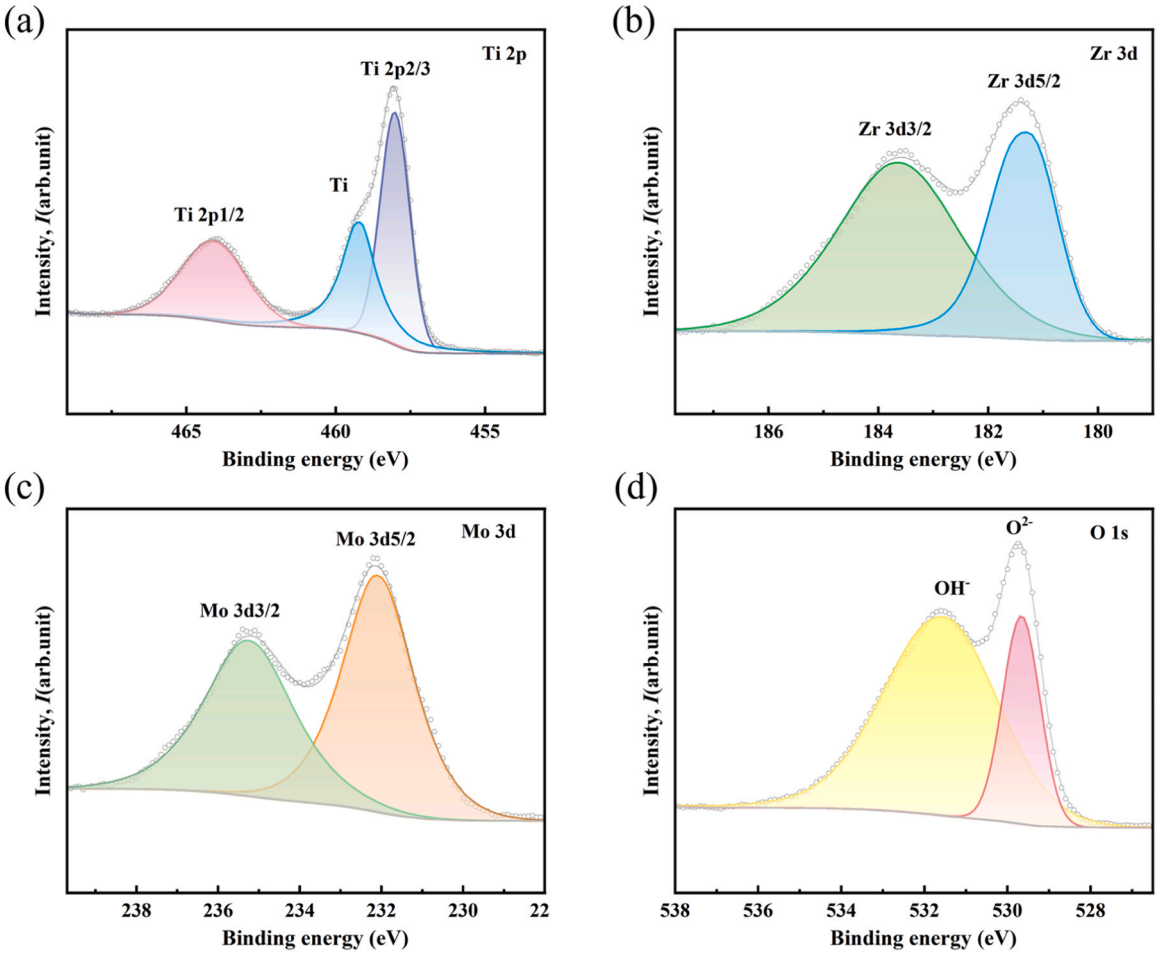

Fig. 12. High-resolution XPS spectra of the external oxide layer surfaces, displaying core-level peaks for (a) Ti 2p, (b) Zr 3d, (c) Mo 3d, and (d) O 1 s.

affinity, facilitating biomolecules and cell interactions, thereby enhancing the bioactivity and osseointegration of the implant material [35].

3.4. Surface hardness

Fig. 13(a) shows surface hardness of Ti–30Zr–5Mo oxide layers after isochronous oxidation at 600–850 °C, with enhanced hardness compared to unoxidized materials (280 Hv). The surface hardness of the Ti–30Zr–5Mo alloy increases gradually with oxidation temperature below 700 °C, reaching a peak of 1075 Hv. This increase is attributed to the formation of hard ceramic phases, such as $ZrTiO_4$ and *m*-ZrO_2. Between 600 °C and 650 °C, the increase in hardness is primarily due to the increased thickness of the oxide layers and the absence of extensive transverse cracking. However, at 850 °C, the hardness decreases due to the formation of an oxide layer mainly composed of the *r*-TiO_2 phase with numerous internal defects. When the double oxide layers formed at 850 °C for 1 h were analyzed separately, the outer layer exhibits a hardness of 876 Hv, while the inner layer reaches 1323 Hv, as shown in Fig. 13(b).

For isothermal oxidation at 600 °C, the surface hardness increases with time, peaking at 1161 Hv after 5 h. This increase is due to the continuous presence of high-hardness phases such as $ZrTiO_4$ and *m*-ZrO_2, with no *r*-TiO_2 formation during this period. After 7 h, the hardness decreases slightly but remains above 1000 Hv, attributed to increased cracking within the oxide layer, which reduces its densification. Compared to isochronous oxidation, the hardness increase during isothermal oxidation is slower, as temperature has a greater impact on the phase evolution of the oxide layer than time.

3.5. Surface roughness

As shown in Fig. 14, the forged Ti–30Zr–5Mo alloy exhibits an initial surface roughness (R_a) of 0.19 μm. This value increases significantly with oxidation temperature, reaching a maximum of 0.48 μm. A moderate increase is observed at 650 °C (R_a = 0.30 μm). During isochronous oxidation, the oxide layer remains uniform and continuous. Below 680 °C, the layers are more uniform, but at higher temperature, larger oxide particles form, leading to small surface fluctuations. Over time, the growth and aggregation of oxide layers further contribute to roughness changes. A temporary decrease in roughness at 2 and 4 h of oxidation is likely due to the smoothing effect of continuous oxide growth [36]. However, as oxidation continues, the roughness increases, reaching 0.34 μm after 7 h. Surface roughness is critical for osteocyte-implant interactions, as microscale roughness values (0.1–100 μm) promotes cell proliferation, differentiation, attachment, and resistance to torque removal [37]. Therefore, thermal oxidation effectively controls implant surface roughness, enhancing its suitability for clinical applications.

3.6. Scratching behaviors

The bonding strength between the oxide layer and the substrate is crucial to ensuring implant durability. Scratching experiments were conducted on oxide layers formed at 650 °C for 1 h to evaluate this property.

The bonding strength was evaluated using three critical loads: L_{c1}, L_{c2} and L_{c3}. L_{c1}, the minimum load for crack initiation (lower critical load), is 17 N. L_{c2}, the load at which delamination begins within the scratch track (the oxide/substrate bonding force), is 43 N. L_{c3}, the load

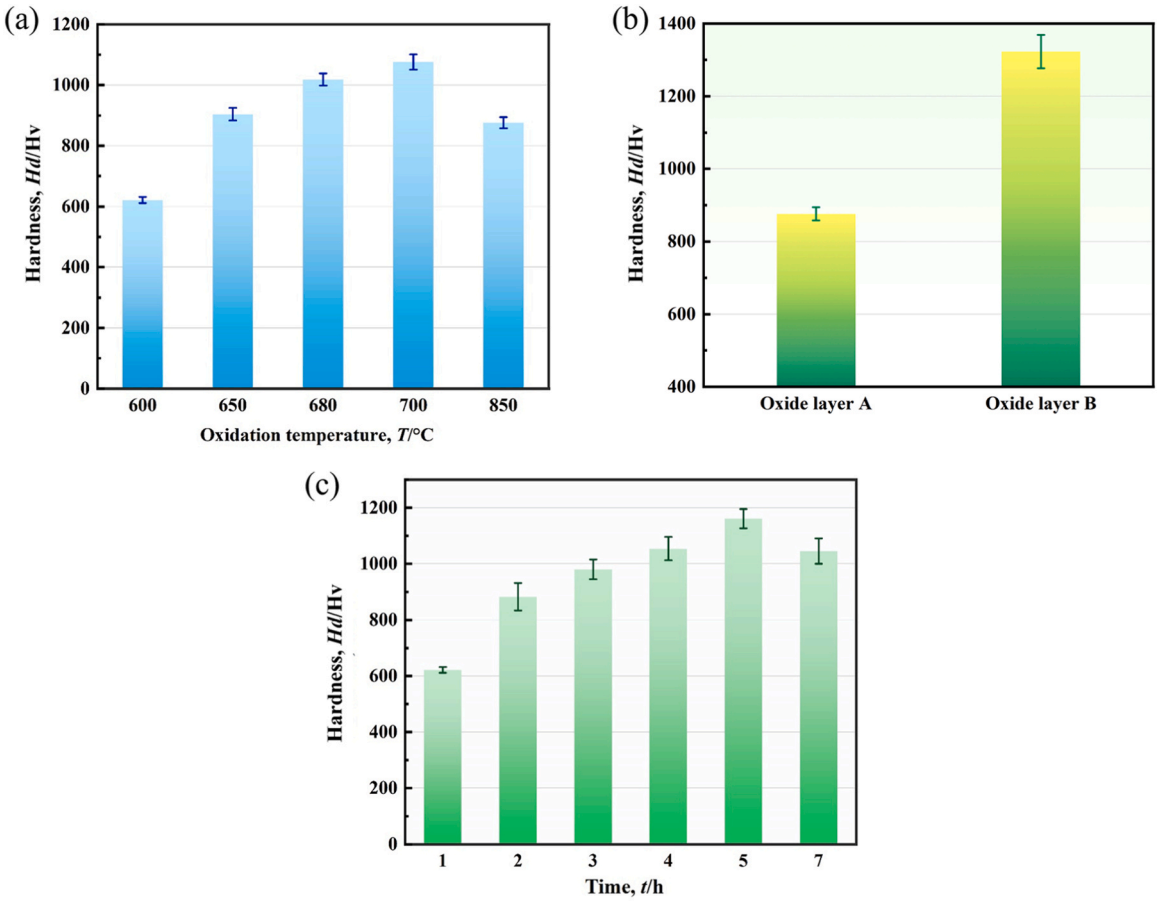

Fig. 13. Microhardness of the oxide layer on Ti–30Zr–5Mo materials: (a) Isochronous oxidation at 600–850 °C for 1 h. (b) Microhardness of double oxide layers formed at 850 °C for 1 h. (c) Isothermal oxidation at 600 °C for 1–7 h.

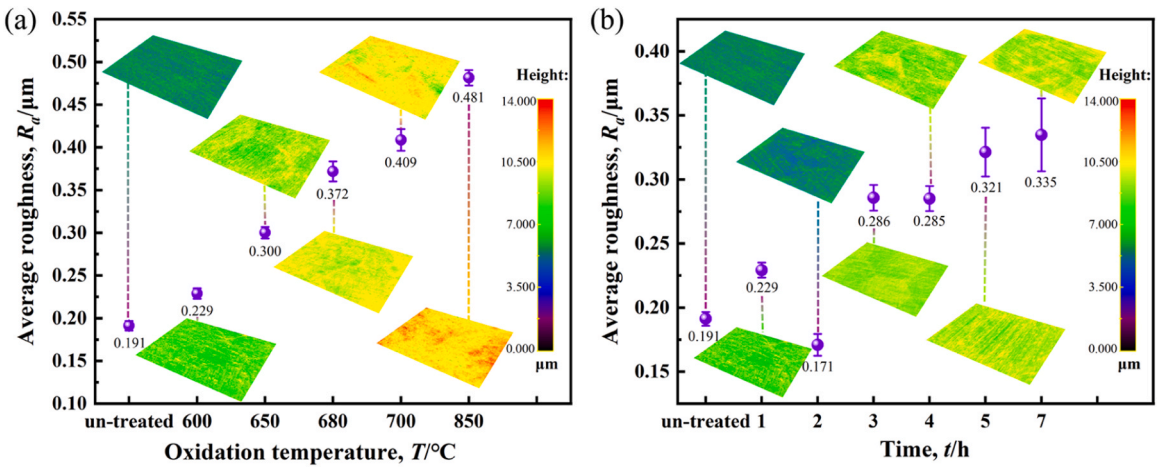

Fig. 14. Surface roughness of Ti–30Zr–5Mo materials after oxidation: (a) Isochronous oxidation at 600–850 °C for 1 h. (b) Isothermal oxidation at 600 °C for 1–7 h. The inserts illustrate the materials' surface topography.

for complete peeling of the oxide layer (higher critical load) is 79 N. These values were determined by abrupt changes in the acoustic emission intensity or tangential friction, along with the scratch morphology, as illustrated in Fig. 15. At L_{c1}, the first crack appears as a mutation in the acoustic emission signal. Beyond L_{c2}, the scratch track widens significantly, with broken oxide debris along the edges; SEM analysis reveals scaly tensile cracks transitioning to uniform plastic deformation as the load increases, accompanied by strong acoustic signals marking delamination onset. At L_{c3}, complete peeling is confirmed by the absence of internal tensile cracking and the presence of homogeneous plastic deformation with the friction curve showing an abrupt slope change.

The toughness of the oxide layers is proportional to L_{c1} and the difference between L_{c3} and L_{c1}. The Scratch Crack Propagation Resistance (CPR_s), defined as

$$CPR_s = L_{c1} \quad (L_{c3} - L_{c1}) \tag{1}$$

quantifies the oxide layer's resistance to crack propagation [38]. For the oxide layer formed at 650 °C for 1 h, the CPRs value is 1057 N^2, indicating excellent toughness compared to other coatings [39]. The oxide layer's strong interfacial adhesion and crack resistance minimize delamination and debris formation under cyclic physiological loads, ensuring implant stability. The failure mode involves through-thickness cracking, manifesting as scaly tensile cracks behind the indenter [40], induced by tensile stresses during indenter sliding and terminate at the interface between the harder oxide layer and the softer substrate [41]. The critical load values are influenced by factors such as oxide layer thickness, surface roughness, and the hardness of both the oxide layer and substrate, which must be carefully controlled to optimize bonding

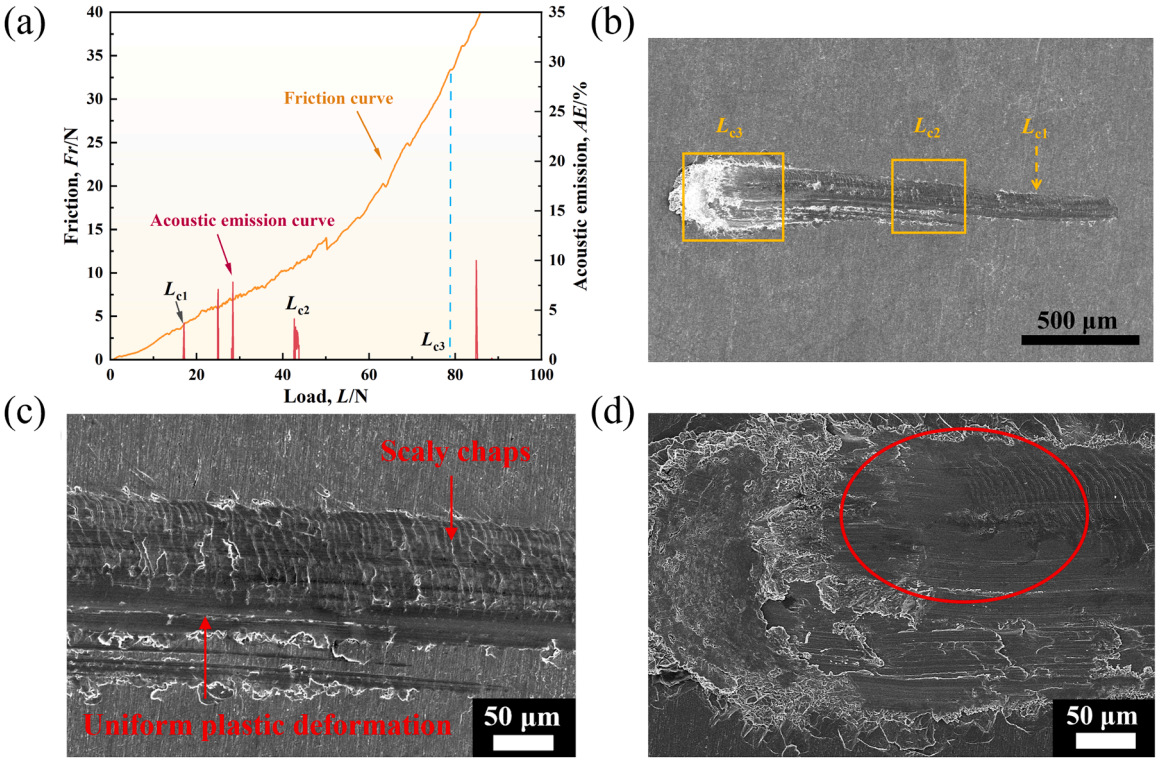

Fig. 15. Scratch test results of Ti–30Zr–5Mo materials oxidized at 650 °C for 1 h: (a) Acoustic emission spectra and friction curve, (b) SEM image of the entire scratch, (c) SEM image at the load corresponding to L_{c2}, and (d) SEM image at the load corresponding to L_{c3}.

strength and toughness.

3.7. Electrochemical corrosion resistance

To assess the effect of the oxide layer on the corrosion resistance of the alloy, the electrochemical behavior of materials with and without the oxide layer (the latter obtained by removing the oxide layer after thermal oxidation at 650 °C for 1 h) was compared in a 0.9 wt% NaCl solution. As shown in Fig. 16(a), both the oxide-covered and oxide-free materials exhibit typical active-passive transitions with a stable passive state across the applied potential range with no sharp current spikes, indicating minimal pitting corrosion, as supported by SEM images in Fig. 17. A gradual current density increases at ~1.2 V (vs. SCE, ~1.85 V vs. RHE) occurs without sharp transpassive spikes, indicating localized passive film dissolution rather than transpassivation. Literature [42] suggests Ti(IV) to Ti(V) or Ti(VI) oxidation requires potential > 7.5 V vs. RHE, far exceeding our test conditions, ruling out this transition. The current density at polarization scan's end was $2.10 \pm 0.20 \times 10^{-6}$ A·cm^{-2} for the oxide-covered samples and $3.17 \pm 0.28 \times 10^{-6}$ A·cm^{-2} for the oxide-free samples. Potentiodynamic polarization curves were analyzed using Tafel extrapolation to determine the corrosion potential (E_{corr}) and corrosion current density (I_{corr}). The oxide-free material exhibits an E_{corr} of -0.397 ± 0.011 V, significantly lower than that of the oxide-covered material (-0.333 ± 0.012 V), indicating a reduced corrosion tendency due to the oxide layer. Moreover, the I_{corr} of the oxide-covered material is $8.96 \pm 0.16 \times 10^{-9}$ A·cm^{-2}, approximately 1/18 that of the substrate ($1.620 \pm 0.58 \times 10^{-7}$ A·cm^{-2}), confirming the oxide layer's substantial reduction of corrosion kinetics. Other Ti–Zr-based alloys subjected to similar oxidation conditions typically exhibit corrosion current densities on the order of 10^{-8} A·cm^{-2} [36,43,44], aligning with the observed results. This similarity likely stems from the formation of dense, ZrO_2-rich oxide layers that provide effective corrosion protection across these systems. The reduced corrosion current density reflects the oxide layer's corrosion resistance, minimizing ion release and enhancing biocompatibility in physiological environments [45].

Oxide-covered materials exhibit slightly lower film failure potential than oxide-free materials. SEM images in Fig. 17 show ~1 μm near-circular pits on both, but fewer on oxidized surfaces, suggesting the oxide layer suppresses pitting. The gradual current rise at ~1.2 V in Fig. 16(a) suggests slow pitting rather than severe film breakdown, confirming protective role of the passive film, especially for oxidized materials, under anodic stress, enhancing corrosion resistance for spinal rods.

Electrochemical impedance spectroscopy (EIS) results in 0.9 wt% NaCl solution are presented in Fig. 16(b–d). The Nyquist plot in Fig. 16 (b) shows a significantly larger impedance arc radius for the oxidized material compared to the base alloy, reflecting higher charge transfer resistance and a lower corrosion rate. The Bode magnitude plot in Fig. 16(c) indicates that, in the medium-to-low frequency range (10^{-2}~10^{2} Hz), the impedance modulus ($|Z|$) of both materials increases with decreasing frequency, with the oxidized material consistently exhibiting higher $|Z|$ values, indicative of superior corrosion protection. In the Bode phase plot (Fig. 16(d)), the oxidized material maintains a phase angle above 80° over a wide frequency range, approaching ideal capacitive behavior, whereas the phase angle of the base alloy decreases in the low-frequency region, indicating inferior passive film protection.

The EIS data were fitted using the equivalent circuit shown in the inset of Fig. 16(b) with Zsimp Win software, with multiple fittings

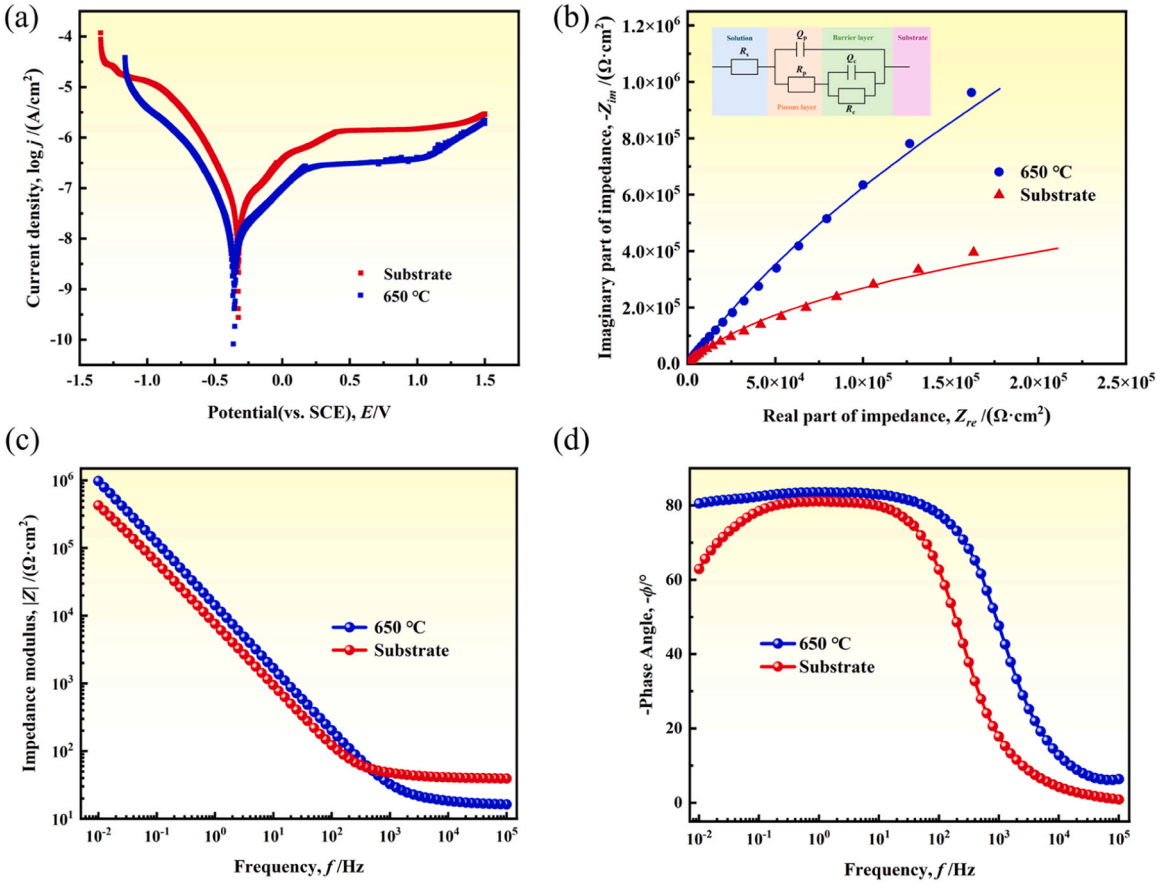

Fig. 16. Electrochemical corrosion test results for the oxide layer and alloy substrate in 0.9 % NaCl solution: (a) Potentiodynamic polarization curves, (b) Nyquist plot, (c) Bode magnitude plot, and (d) Bode phase plot.

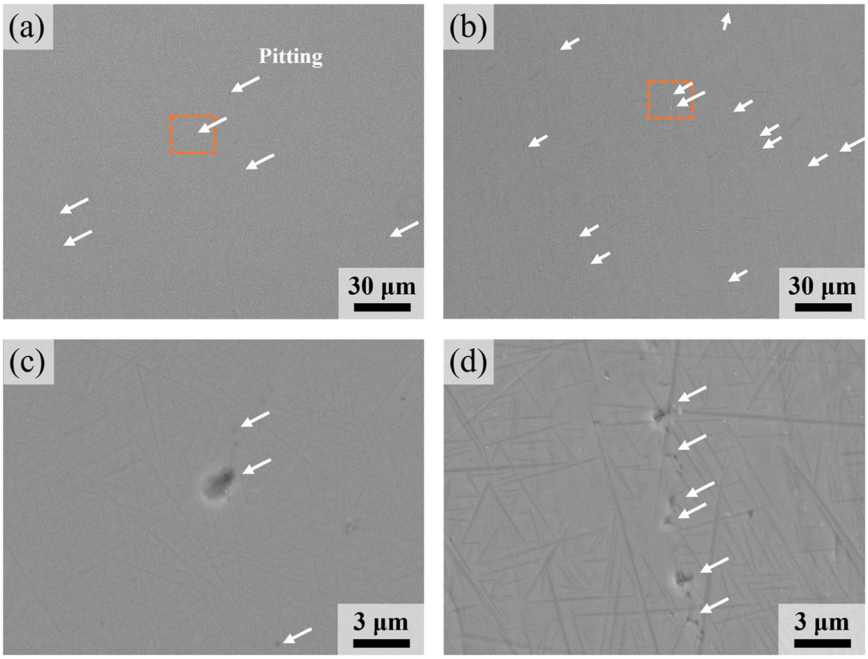

Fig. 17. Surface morphology of Ti–30Zr–5Mo after potentiodynamic polarization in 0.9 % NaCl solution: (a, b) Low-magnification views of oxide-covered and oxide-free surfaces, respectively; (c, d) Corresponding high-magnification images of the boxed areas in (a) and (b).

confirming minimal error. The electrochemical impedance parameters are summarized in Table 2. Here, R_s denotes solution resistance, R_p and R_c represent the porous and barrier layer resistances, respectively, and Q_p and Q_c represent the corresponding capacitance. Titanium alloys typically form a dual-layer passive film in corrosive environments, comprising a dense inner layer and a porous outer layer, corresponding to the barrier and porous layers in the equivalent circuit, respectively [46]. For the oxidized material, the porous layer corresponds to the oxide layer, and the barrier layer represents the oxide-substrate interface [47]. The barrier layer resistance (R_c) exceeds the porous layer resistance (R_p) by approximately five orders of magnitude, contributing significantly to corrosion protection. The R_c value of the oxidized material is 1.37×10^5 Ω·cm^{-2} higher than that of the base alloy, underscoring its enhanced corrosion resistance, consistent with the polarization curve results. The enhanced corrosion resistance stems from a dense, ZrO_2-rich internal oxide layer with high chemical stability and strong substrate adherence, serving as an effective barrier against electrolyte penetration and ion diffusion.

4. Discussion

4.1. Internal oxidation kinetics

Fig. 18 shows internal oxide layer thickness as a function of time (600 °C, 1–7 h), with $k_p = 1.9888$ μm^2/h and $R^2 = 0.7455$, reflecting deviation from parabolic growth due to cracks and grain boundary diffusion. During the first 6 h, the oxidation rate increases gradually, but a noticeable decrease occurs after 7 h. If internal oxidation were solely governed by lattice diffusion of oxygen and alloying elements, it would follow parabolic kinetics, with the rate directly linked to oxygen permeability [29]. However, the nonlinear behavior observed in this study is influenced by multiple factors. Initially, the internal oxide layer is dense, with minimal cracks during the first 3 h. As oxidation progresses, cracks multiply and propagate, creating pathways for rapid oxygen diffusion, which accelerates the oxidation process [48]. This observation is consistent with studies on hot isostatically pressed (HIPed) Zr–2.5 Nb alloys, where crack formation has been shown to increase oxidation rates, particularly in materials oxidized at 550 °C for 3 h [26]. In addition to these structural changes, the substrate

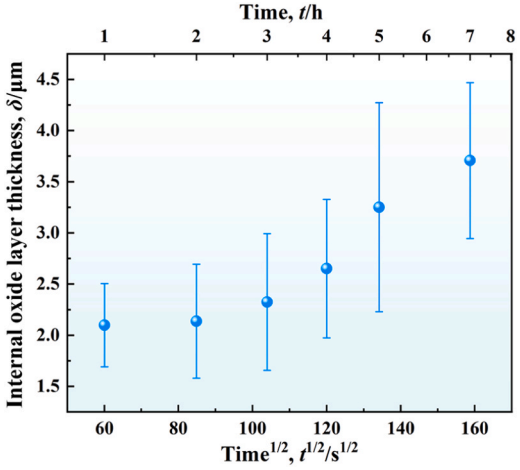

Fig. 18. Relationship between internal oxide layer thickness and the square root of oxidation time.

Table 2
Electrochemical impedance parameters.

Materials	R_s (Ω·cm^{-2})	Q_p (μF·cm^{-2}·s^{n-1})	Q_p-n	R_p (Ω·cm^{-2})	Q_c (μF·cm^{-2}·s^{n-1})	Q_c-n	R_c (Ω·cm^{-2})
Oxide-covered	15.94	4.28	0.9430	8.50	8.62	0.9160	1.620×10^6
Oxide-free	29.70	8.29	0.9705	38.07	15.28	0.8649	1.483×10^6

morphology further influences oxidation kinetics. Local variations in depth at the oxide layer/substrate interface are related to the presence of acicular α phases, which split the β phases into smaller domains, creating numerous grain boundaries. At lower temperatures, these grain boundaries act as fast diffusion channels for oxygen and alloying elements, amplifying grain boundary effects. Consequently, diffusion in this study deviates from classical lattice diffusion, giving rise to non-parabolic internal oxidation kinetics.

4.2. Stability and phase transformation of oxide layers

The oxidation process involves phase transformations, particularly of tetragonal zirconia (*t*-ZrO_2). As shown in Fig. 9(b) and (d), the primary phases in the internal oxide layers are $ZrTiO_4$ and *m*-ZrO_2, with $ZrTiO_4$ content increasing over time. Initially, *t*-ZrO_2 forms but transforms into *m*-ZrO_2 as its instability increases when grain sizes surpass a critical threshold of approximately 30 nm [49]. This critical size can be influenced by factors such as macroscopic and internal stress states, disparities in surface energy, and grain morphology [50]. High stress at the undulations of the oxide/substrate interface stabilizes *t*-ZrO_2 during early oxidation stages. However, as stress accumulates and the oxide layer thickens, the phase transformation from *t*-ZrO_2 to *m*-ZrO_2 is triggered [51]. Rutile titanium dioxide (*r*-TiO_2) forms within the *t*-ZrO_2 lattice, and their shared tetragonal crystal structure facilitates the formation of a solid solution during oxidation. The presence of *r*-TiO_2 promotes the transformation to $ZrTiO_4$, likely via the reaction *t*-ZrO_2+*r*-TiO_2→$ZrTiO_4$. This process is also observed in oxide coatings on Ti-Zr-based alloys subjected to thermal oxidation at 450–500 °C in air [30]. Volume expansion from ZrO_2 structural transformations, differing expansion coefficients in three directions, and hysteretic phase transitions induce strain and stress concentrations within the oxide layer. This, coupled with oxygen incorporation into the substrate, facilitates crack formation [25], which accelerates oxidation by providing short diffusion pathways, especially for Ti atoms [48], making $ZrTiO_4$ the dominant phase. XRD analysis reveals that at 600 °C and 700 °C, *m*-ZrO_2 diffraction peak shifts rightward (~0.28° and ~0.43°, respectively), indicating compressive lattice distortion from transformation-induced stress and constrained volume expansion. Additionally, the increased FWHM suggests inhomogeneous strain within the oxide layer, highlighting stress accumulation's role in driving phase evolution and microstructural refinement.

In contrast to the isothermal oxidation, where *t*-ZrO_2 undergoes significant phase transformation, the combination of an outer oxide layer and elevated temperature at 850 °C enhances the stability of *t*-ZrO_2, allowing it to persist at room temperature within the inner oxide layer. Cracking in the internal oxide layer is significantly reduced compared to lower temperatures due to the protective external oxide layer, further supporting *t*-ZrO_2 stabilization. However, microcracks persist, as internal stress cannot be fully eliminated.

4.3. Oxidation mechanism and growth of double oxide layers

The growth process of the double oxide layer, which reflects oxidation mechanism, is depicted in Fig. 19. Upon exposure to a high-temperature oxidizing atmosphere, oxides of Ti, Zr and Mo form rapidly on the surface. At 850°C, titanium oxides, being more stable, nucleate and grow into a continuous external oxide layer. Meanwhile, the Zr concentration in the alloy remains below the threshold for the transition from internal to external oxidation, allowing ZrO_2 to nucleate and grow toward the substrate interior, resulting in coexisting internal and external oxide layers [52]. Oxygen ions diffuse inward through the external oxide layer, while metallic ions diffuse outward, with faster diffusion of titanium ions due to their smaller radius, thereby promoting the growth of the external oxide layer [30]. ZrO_2 forms preferentially in the internal oxide layer due to its lower enthalpy and higher diffusion rate, leading to Zr depletion. Once the Zr/Ti ratio decreases to a critical level, both Zr and Ti oxidize simultaneously. Inward-diffusing oxygen ions and Zr ions form *t*-ZrO_2, which transforms into $ZrTiO_4$ and *m*-ZrO_2. At high temperatures, the stabilization of *t*-ZrO_2 is facilitated by smaller particle sizes and the external oxide layer, which slows oxygen diffusion into the substrate. Over time, both layers thicken and densify, hindering further oxygen ingress. Prolonged oxidation leads to decomposition and regrowth of the external oxide layer due to oxygen concentration gradients at the interface. This dynamic interaction between the layers affects the oxidation rate, as the external oxide layer supplies oxygen atoms to the substrate, altering the oxygen source for internal oxidation [53].

5. Conclusions

Thermal oxidation effectively enhances the surface properties of Ti–30Zr–5Mo alloys through a novel single-step ambient-air process, leveraging the alloy's low β-transus temperature ($T_\beta \approx 700$ °C) and high Zr content (30 wt%). The effects of oxidation temperature and duration on the oxide layer's morphology, phase constitution, roughness, and hardness were systematically investigated, leading to the following conclusions:

(1) At oxidation temperatures below 680 °C, the internal oxide layers primarily consist of *m*-ZrO_2 and $ZrTiO_4$, with no *r*-TiO_2 formation even after 7 h (at 600 °C). At 850 °C, a two-layer structure forms, comprising a predominant porous *r*-TiO_2 external layer overlying a dense internal layer of *t*-ZrO_2 and $ZrTiO_4$, with the external layer mitigating crack formation in the internal layer.
(2) Surface hardness increases post-oxidation, peaking at 1161 Hv after 5 h at 600 °C, attributed to the formation of a hard ZrO_2-rich layer. Surface roughness increases with higher oxidation temperature and longer durations, reaching up to 0.48 μm, a value considered favorable for osteocyte–implant interactions.
(3) Oxidation at 650 °C for 1 h produces a dense black internal oxide layer with hardness of 904 Hv, roughness of 0.30 μm and adhesion strength of 43 N. Comprising primarily *m*-ZrO_2 and $ZrTiO_4$, this layer exhibits excellent mechanical stability and an 18-fold lower corrosion current density (8.96×10^{-9} vs. 1.62×10^{-7} A·cm^{-2}) compared to the substrate.

These findings highlight that the low T_β enables precise control of oxidation, preventing over-oxidation, while Zr's selective oxidation forms a robust ZrO_2-rich layer that enhances surface properties. This approach significantly improves the suitability of Ti–30Zr–5Mo alloys

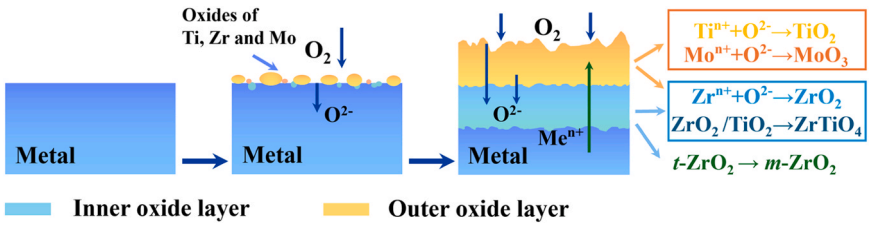

Fig. 19. Schematic illustration of the double oxide layer growth mechanism.

for orthopedic and dental implants and offers insights for vacuum-based oxidation processes, where controlled oxygen partial pressure could further optimize oxide layer properties.

CRediT authorship contribution statement

Xiaoli Zhao: Writing – review & editing, Writing – original draft, Supervision, Project administration, Investigation, Funding acquisition. **Yiming Jin:** Writing – original draft, Investigation, Conceptualization. **Deliang Zhang:** Writing – review & editing, Validation. **Xiaowei Zhang:** Writing – review & editing, Validation. **Takayoshi Nakano:** Writing – review & editing, Validation, Funding acquisition. **Jiani Li:** Writing – original draft, Methodology, Investigation. **Mitsuo Niinomi:** Writing – review & editing, Validation. **Hideki Hosoda:** Writing – review & editing, Validation.

Declaration of Competing Interest

The authors declare that they have no known competing financial interests or personal relationships that could have appeared to influence the work reported in this paper.

Acknowledgement

This work was financially supported by the National Natural Science Foundation of China (Nos. 52071068), the 111 Project, China (B16009) and JST-CREST (No. JPMJCR2194).

Data availability

Data will be made available on request.

References

[1] M. Niinomi, Mechanical properties of biomedical titanium alloys, Mater. Sci. Eng. A. 243 (1998) 231–236, https://doi.org/10.1016/s0921-5093(97)00806-x.
[2] M. Niinomi, M. Nakai, J. Hieda, Development of new metallic alloys for biomedical applications, Acta Biomater. 8 (2012) 3888–3903, https://doi.org/10.1016/j.actbio.2012.06.037.
[3] A.H. Awad, M. Saood, H.A. Aly, A.W. Abdelghany, Role of Mo and Zr additions in enhancing the behavior of new Ti–Mo alloys for implant materials, Met. Mater. Int. 31 (2024) 1232–1253, https://doi.org/10.1007/s12540-024-01813-7.
[4] E. Eisenbarth, D. Velten, M. Muller, R. Thull, J. Breme, Biocompatibility of beta-stabilizing elements of titanium alloys, Biomaterials 25 (2004) 5705–5713, https://doi.org/10.1016/j.biomaterials.2004.01.021.
[5] P.F. Ji, B. Li, B.H. Chen, F. Wang, W. Ma, X.Y. Zhang, M.Z. Ma, R.P. Liu, Effect of Nb addition on the stability and biological corrosion resistance of Ti-Zr alloy passivation films, Corros. Sci. 170 (2020) 108696, https://doi.org/10.1016/j.corsci.2020.108696.
[6] K. Kondoh, M. Fukuo, S. Kariya, K. Shitara, S. Li, A. Alhazaa, J. Umeda, Quantitative strengthening evaluation of powder metallurgy Ti–Zr binary alloys with high strength and ductility, J. Alloy. Compd. 852 (2021) 156954, https://doi.org/10.1016/j.jallcom.2020.156954.
[7] P. Chui, C. Li, J. Wang, Z. Cheng, R. Jing, J. Li, Effect of Zr content on microstructure, mechanical properties and corrosion behaviour in hydrochloric acid for as-cast Ti-Zr alloy, Corros. Sci. 234 (2024) 112136, https://doi.org/10.1016/j.corsci.2024.112136.
[8] P. Mohan, D.K. Rajak, C.I. Pruncu, A. Behera, V. Amigó-Borrás, A.B. Elshalakany, Influence of β-phase stability in elemental blended Ti-Mo and Ti-Mo-Zr alloys, Micron 142 (2021) 102992, https://doi.org/10.1016/j.micron.2020.102992.
[9] X. Zhao, M. Niinomi, M. Nakai, Relationship between various deformation-induced products and mechanical properties in metastable Ti–30Zr–Mo alloys for biomedical applications, J. Mech. Behav. Biomed. Mater. 4 (2011) 2009–2016, https://doi.org/10.1016/j.jmbbm.2011.06.020.
[10] X. Zhao, R. Zhu, W. Song, L. Meng, M. Niinomi, T. Nakano, N. Jia, D. Zhang, A strategy to regulate the yield ratio of a metastable high Zr-containing β titanium alloy: Synergistic effects of the β domain, β stability and β/α interfaces by varying the α phase content, J. Alloy. Compd. 952 (2023) 170024, https://doi.org/10.1016/j.jallcom.2023.170024.
[11] X. Zhao, Y. Wang, H. Xue, N. Jia, Y. Liu, D. Zhang, The effect of strain rate on deformation-induced α′ phase transformation and mechanical properties of a metastable β-type Ti–30Zr–5Mo alloy, J. Alloy. Compd. 894 (2022) 162394, https://doi.org/10.1016/j.jallcom.2021.162394.
[12] C. Wu, X. Zhao, M. Zhang, H. Hosoda, T. Nakano, M. Niinomi, N. Jia, Z. Shao, D. Zhang, Strong grain size effect on tensile behavior of the body-centered-cubic Ti–30Zr–5Mo alloy with stress-induced α′ martensitic transformation, Mater. Sci. Eng. A. 900 (2024) 146455, https://doi.org/10.1016/j.msea.2024.146455.
[13] X. Zhao, M. Niinomi, M. Nakai, T. Ishimoto, T. Nakano, Development of high Zr-containing Ti-based alloys with low Young's modulus for use in removable implants, Mater. Sci. Eng. C. 31 (2011) 1436–1444, https://doi.org/10.1016/j.msec.2011.05.013.
[14] G.T. El-Bassyouni, S.M. Mouneir, A.M. El-Shamy, Advances in surface modifications of titanium and its alloys: implications for biomedical and pharmaceutical applications, Multiscale Multidiscip. Model. Exp. Des. 8 (2025), https://doi.org/10.1007/s41939-025-00823-1.
[15] B. Makurat-Kasprolewicz, A. Ossowska, Recent advances in electrochemically surface treated titanium and its alloys for biomedical applications: A review of anodic and plasma electrolytic oxidation methods, Mater. Today Commun. 34 (2023) 105425, https://doi.org/10.1016/j.mtcomm.2023.105425.
[16] G.S. Rathnam, C. Ratnam, G. Rambabu, Optimizing PVD Coating Parameters for Ti6Al4V Alloy, Rev. Compos. Mater. Av. 33 (2023) 317–328, https://doi.org/10.18280/rcma.330506.
[17] R. Gabor, M. Doubkova, S. Gorosova, K. Malanik, M. Vandrovcova, L. Cvrcek, K. Drobikova, K. Mamulova Kutlakova, L. Bacakova, Preparation of highly wettable coatings on Ti-6Al-4V ELI alloy for traumatological implants using micro-arc oxidation in an alkaline electrolyte, Sci. Rep. 10 (2020) 19780, https://doi.org/10.1038/s41598-020-76448-w.
[18] P. Behzadi, M. Badr, A. Zakeri, Duplex surface modification of pure Ti via thermal oxidation and gas nitriding: Preparation and electrochemical studies, Ceram. Int. 48 (2022) 34374–34381, https://doi.org/10.1016/j.ceramint.2022.08.016.
[19] L. Mohan, C. Anandan, N. Rajendran, Effect of plasma nitriding on structure and biocompatibility of self-organised TiO_2 nanotubes on Ti–6Al–7Nb, RSC Adv. 5 (2015) 41763–41771, https://doi.org/10.1039/C5RA05818J.
[20] Y. Sasikumar, K. Indira, N. Rajendran, Surface modification methods for titanium and its alloys and their corrosion behavior in biological environment: a review, J. BioTriboCorros. 5 (2019) 36, https://doi.org/10.1007/s40735-019-0229-5.
[21] S. Thanigaivel, A. Priya, D. Balakrishnan, K. Dutta, S. Rajendran, M. Soto-Moscoso, Insight on recent development in metallic biomaterials: Strategies involving synthesis, types and surface modification for advanced therapeutic and biomedical applications, Biochem. Eng. J. 187 (2022) 108522, https://doi.org/10.1016/j.bej.2022.108522.
[22] M. Le Saux, J.-C. Brachet, V. Vandenberghe, A. Ambard, R. Chosson, Breakaway oxidation of zirconium alloys exposed to steam around 1000 °C, Corros. Sci. 176 (2020), https://doi.org/10.1016/j.corsci.2020.108936.
[23] M. Richter, H. Matusiewicz, Review of the local tissue reaction to metallic spinal implant debris: Ions and nanoparticles, World J. Adv. Res. Rev. 9 (2021) 167–187, https://doi.org/10.30574/wjarr.2021.9.3.0085.
[24] Z. Shen, D. Tweddle, H. Yu, G. He, A. Varambhia, P. Karamched, F. Hofmann, A. J. Wilkinson, M.P. Moody, L. Zhang, Microstructural understanding of the oxidation of an austenitic stainless steel in high-temperature steam through advanced characterization, Acta Mater. 194 (2020) 321–336, https://doi.org/10.1016/j.actamat.2020.05.010.
[25] L. Kurpaska, J. Favergeon, L. Lahoche, G. Moulin, M.E. Marssi, J.-M. Roelandt, Zirconia layer formed by high temperature oxidation of pure zirconium: stress generated at the zirconium/zirconia interface, Oxid. Met. 79 (2013) 261–277, https://doi.org/10.1007/s11085-012-9348-9.
[26] C. Wang, X. Zhao, S. Li, L. Liu, D. Zhang, M. Niinomi, Low-cost surface modification of a biomedical Zr-2.5Nb alloy fabricated by electron beam melting, J. Mater. Sci. Technol. 143 (2023) 178–188, https://doi.org/10.1016/j.jmst.2022.09.046.
[27] X. Wang, Y. Zhang, W. Han, Design of high strength and wear-resistance β-Ti alloy via oxygen-charging, Acta Mater. 227 (2022) 117686, https://doi.org/10.1016/j.actamat.2022.117686.
[28] A. Behera, S. Nag, K. Mahdak, H. Mohseni, J. Tiley, R. Banerjee, Influence of oxygen ingress on fine scale precipitation of α-Ti during oxidation of Beta21S β-Ti alloy, J. Mater. Sci. 48 (2013) 6700–6706, https://doi.org/10.1007/s10853-013-7470-y.
[29] R.A. Rapp, Kinetics, microstructures and mechanism of internal oxidation - its effect and prevention in high temperature alloy oxidation, Corrosion 21 (1965) 382–401, https://doi.org/10.5006/0010-9312-21.12.382.
[30] W. Wang, W. Cui, Z. Xiao, G. Qin, The improved corrosion and wear properties of Ti-Zr based alloys with oxide coating in simulated seawater environment, Surf. Coat. Technol. 439 (2022) 128415, https://doi.org/10.1016/j.surfcoat.2022.128415.
[31] N. Birks, G.H. Meier, F.S. Pettit. Introduction to the High Temperature Oxidation of Metals, second ed., Cambridge university press, New York, 2006.
[32] Y. Ding, S. Liu, C. Xia, X. Zou, D. Liu, Y. Wang, T. Yang, Q. Li, Thermal oxidation of novel Zr–Ti–Al–V alloy with high strength and toughness and its influence on the corrosion behavior, Surf. Coat. Technol. 423 (2021) 127576, https://doi.org/10.1016/j.surfcoat.2021.127576.
[33] S. Anisah, M. Kanezashi, H. Nagasawa, T. Tsuru, Effect of the Ti/Zr ratio on the hydrothermal and chemical stability of TiO_2-ZrO_2 nanofiltration membranes, Sep. Purif. Technol. 274 (2021), https://doi.org/10.1016/j.seppur.2021.119060.
[34] S. Shousha, S. Khalil, M. Youssef, Tuning metal oxide defect chemistry by thermochemical quenching, Phys. Chem. Chem. Phys. 22 (2020) 6308–6317, https://doi.org/10.1039/c9cp06660h.
[35] J. Quinn, R. McFadden, C.W. Chan, L. Carson, Titanium for Orthopedic Applications: An Overview of Surface Modification to Improve Biocompatibility and Prevent Bacterial Biofilm Formation, iScience 23 (2020) 101745, https://doi.org/10.1016/j.isci.2020.101745.

[36] D. Correa, C. Grandini, L. Rocha, J. Proença, L. Sottovia, N. Cruz, E. Rangel, T. Hanawa, Effect of temperature on thermal oxidation behavior of biomedical Ti-Zr-Mo alloys, J. Alloy. Compd. 905 (2022) 164202, https://doi.org/10.1016/j.jallcom.2022.164202.
[37] J.M. Cordeiro, V.A.R. Barão, Is there scientific evidence favoring the substitution of commercially pure titanium with titanium alloys for the manufacture of dental implants? Mater. Sci. Eng. C. 71 (2017) 1201–1215, https://doi.org/10.1016/j.msec.2016.10.025.
[38] S. Zhang, D. Sun, Y. Fu, H. Du, Effect of sputtering target power on microstructure and mechanical properties of nanocomposite nc-TiN/a-SiN_x thin films, Thin Solid Films 447-448 (2004) 462–467, https://doi.org/10.1016/s0040-6090(03)01125-8.
[39] Y.X. Wang, S. Zhang, Toward hard yet tough ceramic coatings, Surf. Coat. Technol. 258 (2014) 1–16, https://doi.org/10.1016/j.surfcoat.2014.07.007.
[40] S.J. Bull, Failure modes in scratch adhesion testing, Surf. Coat. Technol. 50 (1991) 25–32, https://doi.org/10.1016/0257-8972(91)90188-3.
[41] S.J. Bull, E.G. Berasetegui, An overview of the potential of quantitative coating adhesion measurement by scratch testing, Tribol. Int. 39 (2006) 99–114, https://doi.org/10.1016/j.triboint.2005.04.013.
[42] A. Kazuhisa, O. Toshiaki, Breakdown Phenomena of Anodic Oxide Films on Titanium, Corros. Eng. 46 (1997) 384–390, https://doi.org/10.3323/jcorr1991.46.384.
[43] X. Xu, Z. Li, W. Lai, B. Wang, Q. Xu, Z. Zhang, D. You, W. Li, X. Wang, Improved wear and corrosion resistance of biomedical TiZrNbTaMo medium-entropy alloy by thermal oxidation treatment, Tribol. Int. 189 (2023), https://doi.org/10.1016/j.triboint.2023.108897.
[44] S. Chang, Z. Li, Effect of oxidation at an elevated temperature on the evolution of phases, microstructure, and properties of the oxide films formed on the surface of TiZr, Sci. Rep. 13 (2023), https://doi.org/10.1038/s41598-023-32377-y.
[45] S. Saha, W. Lestari, C. Dini, M.N. Sarian, H. Hermawan, V.A.R. Barão, C. Sukotjo, C. Takoudis, Corrosion in Mg-alloy biomedical implants- the strategies to reduce the impact of the corrosion inflammatory reaction and microbial activity, J. Magnes. Alloy. 10 (2022) 3306–3326, https://doi.org/10.1016/j.jma.2022.10.025.
[46] H. Liu, J. Yang, X. Zhao, Y. Sheng, W. Li, C.-L. Chang, Q. Zhang, Z. Yu, X. Wang, Microstructure, mechanical properties and corrosion behaviors of biomedical Ti-Zr-Mo-xMn alloys for dental application, Corros. Sci. 161 (2019) 108195, https://doi.org/10.1016/j.corsci.2019.108195.
[47] T. Song, S. Liu, B. Chen, Z. Cui, X. Zou, S. Zhang, Q. Li, C. Xia, Enhanced corrosion and wear resistance via thermal oxidation treatment on Zr-2.5 Nb alloy for implant applications, Surf. Coat. Technol. 458 (2023) 129365, https://doi.org/10.1016/j.surfcoat.2023.129365.
[48] V. Maurice, G. Despert, S. Zanna, P. Josso, M.-P. Bacos, P. Marcus, XPS study of the initial stages of oxidation of α_2-Ti_3Al and γ-TiAl intermetallic alloys, Acta Mater. 55 (2007) 3315–3325, https://doi.org/10.1016/j.actamat.2007.01.030.
[49] R.C. Garvie, The occurrence of metastable tetragonal zirconia as a crystallite size effect, J. Phys. Chem. 69 (1965) 1238–1243, https://doi.org/10.1021/j100888a024.
[50] W. Qin, C. Nam, H. Li, J. Szpunar, Tetragonal phase stability in ZrO_2 film formed on zirconium alloys and its effects on corrosion resistance, Acta Mater. 55 (2007) 1695–1701, https://doi.org/10.1016/j.actamat.2006.10.030.
[51] J. Liao, J. Zhang, W. Zhang, F. Xu, Z. Yang, G. Ran, Q. Peng, S. Qiu, Critical behavior of interfacial t-ZrO_2 and other oxide features of zirconium alloy reaching critical transition condition, J. Nucl. Mater. 543 (2021) 152474, https://doi.org/10.1016/j.jnucmat.2020.152474.
[52] F. Gesmundo, F. Viani, Transition from internal to external oxidation for binary alloys in the presence of an outer scale, Oxid. Met. 25 (1986) 269–282, https://doi.org/10.1007/bf01072908.
[53] S. Liu, Y. Liu, X. Jin, W. Mao, G. Wu, Insight into scale transformation and internal oxidation mechanism of hot rolled Si Mn added high strength steel, Mater. Charact. 203 (2023) 113084, https://doi.org/10.1016/j.matchar.2023.113084.